Geofísica Internacional

Revista Trimestral Publicada por el Instituto de Geofísica de la
Universidad Nacional Autónoma de México

— Geofísica Internacional —

Contents

An intraslab earthquake at a depth of 100 km in the subducting Cocos plate beneath Nevado de Toluca volcano

Shri K. Singh, Xyoli Pérez-Campos, Víctor Hugo Espindola, Arturo Iglesias, Luis Quintanar

Resumen

La sismicidad en la placa de Cocos subducida por debajo de México central, definida por sismos moderados y grandes, cesa antes de al frente volcánico activo. No se ha localizado algún sismo intraplaca por debajo de los volcanes Nevado de Toluca y Popocatépetl. En este trabajo se reporta un evento de $M_w3.3$ a una profundidad de 98 km, a 38 km al oeste del Nevado de Toluca. Este evento provee evidencia, por primera vez, de un sismo en la placa subducida a profundidad de ~100 km por debajo del volcán. Registros de este evento también proveen evidencia de una alta atenución de las ondas de cizalla conforme se propagan a través de la cuña del manto astenosférico. Es posible que la sismicidad intraplaca por debajo de los volcanes activos en México central, a un nivel de M ~3, sea abundante pero que no ha sido documentada en el pasado por la falta de instrumentación en la región.

Palabras clave: sismicidad intraplaca, Nevado de Toluca, mando astenosférico, México.

Abstract

Seismicity in the subducted Cocos plate below central Mexico, defined by moderate and large earthquakes, ceases well before reaching the active volcanic front. No intraslab earthquake has been reliably located below Nevado de Toluca and Popocatepetl volcanos. Here we report on an $M_w3.3$ event at a depth of 98 km, 38 km to the west of Nevado de Toluca. The event provides evidence, for the first time from an earthquake, of subducted slab at a depth of ~ 100 km below the volcano. Recordings of the event also provide evidence of high attenuation of shear waves as they propagate through the mantle-wedge asthenosphere. It is possible that intraslab seismicity beneath active volcanoes in central Mexico at M ~3 level is abundant but has not been documented in the past because of poor instrumentation.

S.K. Singh*
Instituto de Geofísica
Universidad Nacional Autónoma de México
Ciudad Universitaria
Alcaldía Coyoacán 04510
México CDMX, México
*Corresponding author:krishnamex@yahoo.com

Xyoli Pérez-Campos
Servicio Sismológico Nacional
Instituto de Geofísica
Universidad Nacional Autónoma de México
Ciudad Universitaria
Alcaldía Coyoacán 04510
México CDMX, México

Víctor Hugo Espindola
Servicio Sismológico Nacional
Instituto de Geofísica
Universidad Nacional Autónoma de México
Ciudad Universitaria
Alcaldía Coyoacán 04510
México CDMX, México

Arturo Iglesias
Instituto de Geofísica
Universidad Nacional Autónoma de México
Ciudad Universitaria
Alcaldía Coyoacán 04510
México CDMX, México

Luis Quintanar
Servicio Sismológico Nacional
Instituto de Geofísica
Universidad Nacional Autónoma de México
Ciudad Universitaria
Alcaldía Coyoacán 04510
México CDMX, México

S. K. Singh, X. Pérez-Campos, V. H. Espindola, A. Iglesias, L. Quintanar

Introduction

Intraslab seismicity defines the geometry of the subducting plates and sheds light on its thermal structure. In central Mexico, this seismicity ceases well before reaching the active volcanic front (Pardo and Suárez, 1995). For example, a seismicity section from the middle America trench passing through the Nevado de Toluca volcano (N21ºE), reveals that the intraslab earthquake activity ends at a depth of about 70 km, ~ 240 km from the trench and ~ 80 km from the volcano (Figure 1). A similar section from the trench through Popocatépetl shows that these events reach a depth of about 55 km and cease to occur ~ 240 km from the trench about 80 km from the volcano (Figure 1). Until now no intraslab earthquake has been reliably located whose epicenter lies near these active volcanoes. Here we report an intraslab earthquake which occurred on 19 May 2015 about 38 km west of the Nevado de Toluca at a depth of 98 km. The event provides first evidence from an earthquake that the Cocos plate is at a depth of ~ 100 km beneath the Nevado de Toluca volcano. The recordings also provide evidence of high attenuation of shear waves as they propagate through the mantle-wedge asthenosphere between the subducting Cocos plate and the continental crust.

Towns and cities in the Mexican altiplano are exposed seismic hazard from interplate earthquakes on the subduction thrust, crustal earthquakes in the Mexican Volcanic Belt (MVB), and intraslab earthquake in the subducted Cocos plate. The 19 September 2017 (M_w7.1) Morelos-Puebla earthquake is the most recent example of the intraslab event which destroyed many villages and towns in the epicentral region. It was the second most destructive earthquake in the history of Mexico City, next only to the 1985 (M_w8.0) interplate earthquake. The earthquake was located to the SSE of Mexico City at an epicentral distance of 114 km from Ciudad Universitaria (18.41 ºN, 98.71 ºW; depth H = 57 km). It is the closest, reliably located, intraslab earthquake (large or small) to Mexico City. One of many questions raised in the wake of the destruction left by the earthquake is whether a similar earthquake can occur at closer distance to Mexico City albeit at somewhat greater depth (Singh *et al.*, 2018). In this context, the detection and analysis of small intraslab earthquakes below the Central Mexican Volcanic Belt, such as the 19 May 2015 event, attains further importance.

Location and focal mechanism

Although the earthquake was small, it was reasonably well recorded by an accelerographic station in the epicentral region (TEJU, Figure 1b), and many broadband stations of the Servicio Sismológico Nacional (SSN, Mexican National Seismological Service; Pérez-Campos *et al.*, 2018; SSN, 2018) and the newly-completed Valley of Mexico network (Quintanar *et al.*, 2018). Figure 2 shows EW velocity seismograms at the closest 4 stations with clear signal. The accelerogram at TEJU was high-pass filtered at 1 Hz and then integrated to obtain the velocity trace shown in the figure. From the location of these stations (Figure 1b) and the (S-P) times on the seismograms, it is clear that the event was relatively deep. We examined recordings at 31 stations within an epicentral distance of 360 km and found useful phase data at 19 stations. *S-phase* was read on the transverse component. The earthquake was located using 19 *P*-phase and 6 *S-phase* arrival times, and the crustal model used by the SSN. The depth, H, was varied between 0 and 200 km. A sharp minimum in the rms residual (0.31 s) occurs at H = 98 km. The final solution is: 19.092 ºN, 100.131 ºW; H = 98.2 km; origin time 03:06:53.9; azimuthal gap = 1580; and estimated errors in latitude, longitude, and H of 3.9 km, 3.3 km, and 3.3 km, respectively. The epicenter of the 19 May 2015 earthquake is 38 km to the west of Nevado de Toluca.

The first motions could be read at 9 stations, which yields a normal-faulting focal mechanism (Figure 3): fault plane 1 with strike 316º, dip 46º, rake -90º; fault plane 2 with strike 116º, dip 46º, rake -90º. We note that the solution is not well constrained.
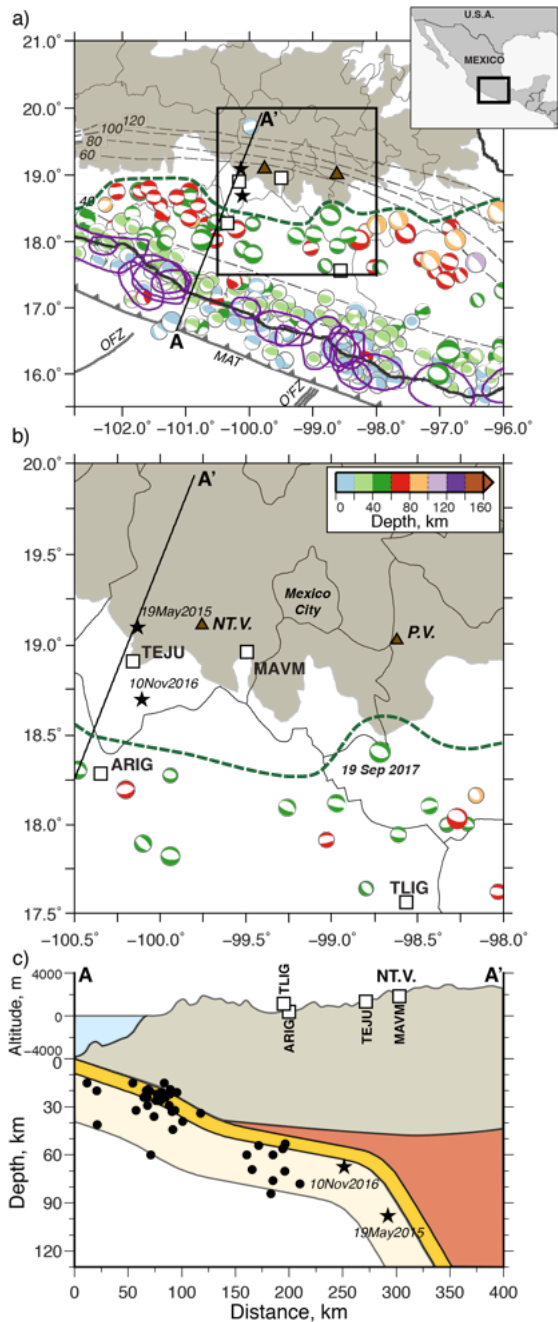
Figure 1. (a) Tectonic and location map (modified from Singh *et al.*, 2018). Focal mechanisms and epicenters of earthquakes from Global CMT catalog with some exceptions. Event 1 is the intraslab Morelos-Puebla earthquake of 19 September 2017 (Mw7.1). Color of the focal mechanism is keyed to the depth of the event. Black stars: intraslab earthquakes studied here. Black dashed lines: depth contours of the Benioff zone as compiled by Ferrari *et al.* (2012). Thick green dashed line defines the observed limit of moderate- and large-magnitude intraslab seismicity. Aftershock areas of large interplate earthquakes are shown in magenta color. Shaded area: Trans Mexican Volcanic Belt (Ferrari *et al.*, 2012). (b) Enlarged view of the rectangular area marked in (a), showing

location of four stations whose data is analyzed in this study and the epicenters of 2015 (Mw3.3) and 2016 (M4.1) earthquakes. NT. V.: Nevado de Toluca volcano. P. V.: Popocatépetl volcano. (c) Section along line AA' shown in (a) and (b). The seismicity within ± 50 km of AA' and the stations are projected on the section. USL: ultra slow-velocity layer at the top of subducting oceanic crust shown in orange (Song *et al.*, 2009; Pérez-Campos *et al.*, 2008). Brick color: mantle-wedge asthenosphere.

The SSN catalog lists an earthquake on 10 November 2016 (*M*4.1), ~ 45 km south of the 2015 epicenter. We relocated this event following the same procedure as for the 2015 event. The event was located using 15 *P-phase* and 7 *S-phase* arrival times. The minimum rms residual (0.39 s) occurs at H = 68 km. The final solution is: 18.687 ºN, 100.120 ºW; H = 67.6 km; origin time 08:23:50.7; azimuthal gap = 660; and estimated errors in latitude, longitude, and H of 1.8 km, 2.5 km, and 4.1 km, respectively.

The earthquakes of 2016 and 2015 are 250 km and 290 km from the trench, respectively (Figure 1). The intraslab seismicity limit, defined by the Global CMT locations (shown in dashed green line in Figure 1) ends about 220 km from the trench. We note, however, that the teleseismic locations of Mexican earthquakes are systematically shifted by ~ 30 km to the NE (Singh and Lermo, 1985; Hjörleifsdóttir *et al.*, 2016). If we take into account this mislocation, the intraslab seismicity limit defined by previous moderate and large earthquakes may be ~ 190 km from the trench. The events of 2015 and 2016 demonstrate that low-magnitude intraslab seismicity does persist beyond 190 km.

The focal depth of the 2016 earthquake agrees with the 60 km-depth contour of the Benioff zone. This is also true for the 19 September 2017 (*M*w7.1; H = 57 km) earthquake (Figure 1). Generally, the hypocenters of well-located small/moderate intraslab earthquakes in central Mexico are less than 15 km below the plate interface (e.g., Pacheco and Singh, 2010). If we assume that the closest distance of the plate interface from the 2016 and 2015 events is 15 km then the depth of the slab increases by ~ 40 km within ~ 40 km, a dramatic change in dip
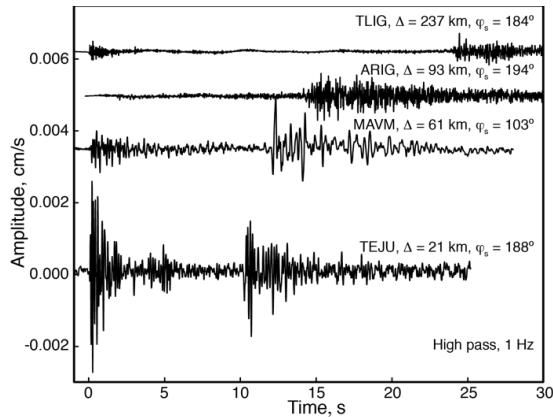
Figure 2. EW velocity seismograms at the four closest stations with clear signal. Visual examination of the seismograms suggests a relative high-frequency deficiency at TEJU and MAVM as compared to ARIG and TLIG.

Figure 3. Normal-faulting focal mechanism which fits the first-motion data.

over a short distance (Figure 1c). Generally, the dip of T axis in subducted slabs coincides with the dip of the slab (see, e.g., Pardo and Suárez, 1995 and Pacheco and Singh, 2009 for the Mexican subduction zone). Thus, the horizontal orientation of T-axis of the 2015 earthquake is not consistent with a steeply-dipping slab. We recall, however, that the focal mechanism is not well constrained. Clearly, locating more intraslab events in the region is critical to mapping the detailed geometry of the subducting Cocos plate as it changes its dip and plunges in the asthenosphere.

Source Spectrum and Q

The source acceleration spectrum of the earthquake, $f^2 \dot{M}_0(f)$, was estimated from the analysis of the S wave at the four stations. The method is described elsewhere (Singh *et al.*, 1999); only a brief description is given here. The geometrical mean of Fourier acceleration spectral amplitude, $A(f, R)$, of the two horizontal components of ground motion at a station may be written as:

$$A(f,R) = 0.78 \left[(2\pi)^2 \big/ (4\pi\rho\beta^3) \right] f^2 \dot{M}_0(f) G(R) e^{-\pi f R / \beta Q(f)} \quad (1)$$

where $\dot{M}_0(f)$, the source displacement spectrum or the moment rate spectrum, tends to M_0 as $f \to 0$, R = hypocentral distance, ρ = density in the focal region (taken as 3.2 g/cm³), β = shear-wave velocity in the focal region

Figure 4. Median horizontal Fourier spectra of S-wave at stations TEJU, MAVM, ARIG, and TLIG. Comparison of shapes and amplitudes of the spectra at higher frequencies suggest much greater attenuation of high-frequency S waves along the paths from source to TEJU and MAVM.

(taken as 4.68 km/s), and $Q(f)$ = quality factor, which includes both anelastic absorption and scattering. Following García *et al.* (2004), the geometrical spreading term, $G(R)$, in Equation (1) was taken as $1/R$. Appropriate $Q(f)$ for the earthquake is the one derived by García *et al.* (2004) for intraslab earthquakes in Mexico; i.e., $Q(f) = 251 f^{0.58}$. However, the acceleration spectra, $A(f)$, at the four stations, shown in Figure 4, suggest that Q for paths to ARIG and TLIG is very different from that for paths to TEJU

and MAVM (Figure 1). To further appreciate this difference, we first used $Q(f) = 251f^{0.58}$ to correct spectra at all four stations and computed .The median source acceleration spectrum and ± one standard deviation curves are shown in Figure 5a. We note that the standard deviation is extremely large at high frequencies ($f>8$ Hz), strongly suggesting that the same Q is not adequate for all paths.

Based on the similarity of the spectra in Figure 4, we then formed two groups. One group consisted of ARIG and TLIG and the other group included TEJU and MAVM. We computed the source acceleration spectrum for ARIG and

TLIG group using $Q(f) = 251f^{0.58}$ (Figure 5b). We interpreted the median spectrum by Brune ω^2-source model (Brune, 1970) and obtained an estimate of seismic moment (M_0) and corner frequency (f_c). The spectrum is well fit with $M_0 = 1.14 \times 10^{14}$ Nm ($M_w 3.3$) and $f_c = 8.4$ Hz (Figure 5b). The stress drop ($\Delta\sigma$) computed using the Brune model (Brune, 1970) is 5.5 MPa. As expected, the theoretical spectrum for a Brune source model with $M_0 = 1.14 \times 10^{14}$ Nm ($M_w 3.3$) and $f_c = 8.4$ Hz does not fit the median spectrum of the TEJU and MAVM group at high frequencies ($f > 5$ Hz) if $Q(f) = 251f^{0.58}$ is used for attenuation correction in equation 1 (Figure 5c).
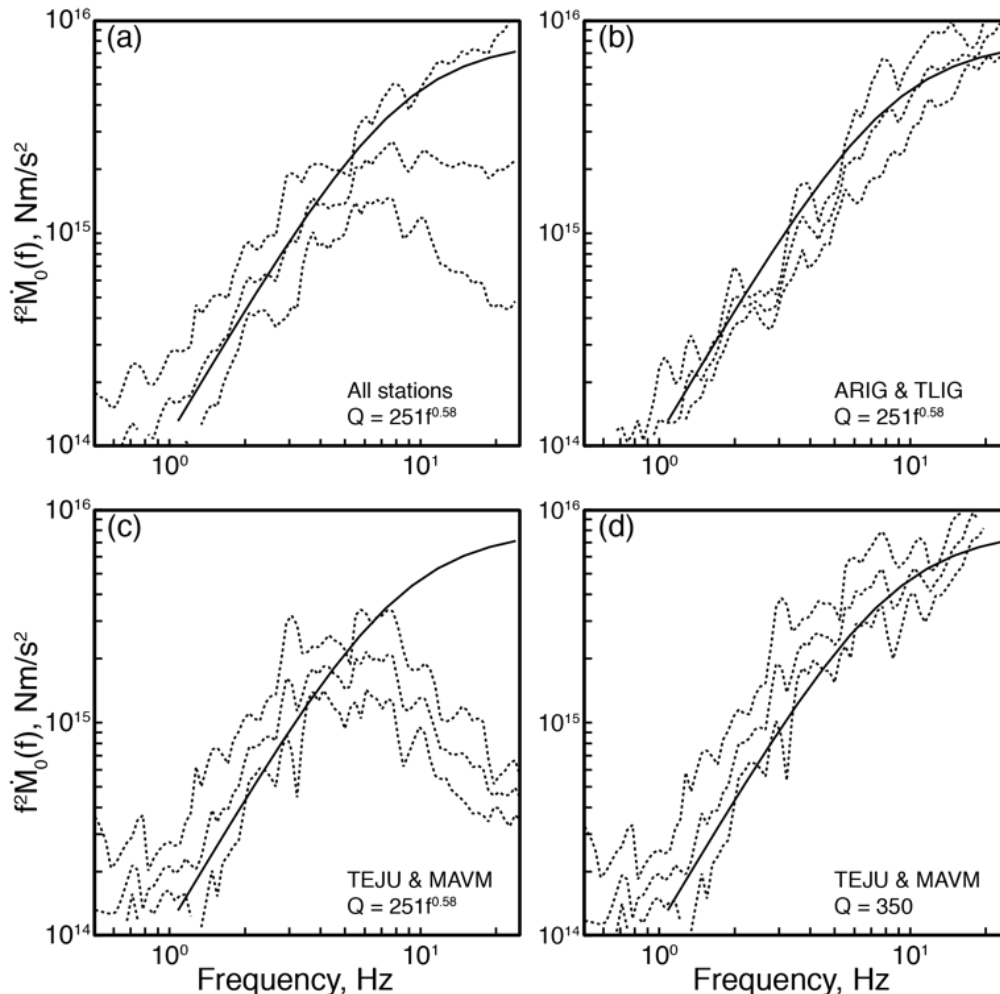
Figure 5. Median source acceleration spectrum, $f^2 \dot{M}_0(f)$, and ± one standard deviation curves. (a) Source spectrum using recordings from all four stations and $Q(f) = 251f^{0.58}$. (b) Source spectrum using recordings from ARIG and TLIG and $Q(f) = 251f^{0.58}$. (c) Source spectrum using recordings from TEJU and MAVM and $Q(f) = 251f^{0.58}$. (d) Source spectrum using recordings of TEJU and MAVM and $Q = 350$. In (a) to (d) the theoretical curve (continuous line) corresponds to Brune ω2-source model with M0 = 1.14x10^{14} Nm (Mw3.3) and fc = 8.4 Hz.

If we assume that ω^2-source model is appropriate for the earthquake, and M_0 and f_c obtained for the ARIG and TLIG group correctly describes the source, then $Q = 350$ ($1.0 \leq f \leq 20$ Hz) for paths to TEJU and MAVM roughly fit the observed median spectrum (Figure 5d). We note that this Q is 0.25 and 0.37 of $Q = 251f^{0.58}$ at $f = 20$ and 10 Hz, respectively. The two Qs are equal at $f = 1.8$ Hz. Shapiro et $al.$ (2000) reported that shear waves traversing Popocatépetl volcano were highly attenuated. However, no such attenuation was discernible in the case of Nevado de Toluca. Thus, the relatively low Q (high attenuation) along the path to TEJU and MAVM is probably a consequence of shear-wave propagation through the mantle-wedge asthenosphere between the subducting Cocos plate and the continental crust. In any case, the paths to TEJU and MAVM for this earthquake do not cross the volcanic edifice (Figure 1).

Low Q in the mantle wedge in Mexico has been previously reported by Singh et $al.$ (2006). Q of the mantle wedge below Japan has been mapped in great detail (see e.g., Takanami et $al.$, 2000; Tsumura et $al.$, 2000), thanks to high density of seismic stations and their favorable location with respect to intraslab seismicity. Low Q of the mantle wedge implies large attenuation of seismic waves reaching the back arc. An impressive demonstration of this comes from the extensive recordings of Japanese inslab earthquakes. A rather low Q for S waves (~60) in the mantle wedge is required to explain recorded seismic waves on the western seaboard of Japan, across the volcanic front, as compared to eastern Japan where the high-frequency seismic waves propagate through the subducted slab and the continental lithosphere with much less attenuation.

Conclusions

Intraslab earthquakes are linked to metamorphic dehydration reactions in the minerals of subducting oceanic crust and upper mantle (e.g., Kirby et $al.$, 1996; Hacker et $al.$, 2003). Thus, a lack of intraslab seismicity in the "warm" subducting Cocos plate (age near the trench is ~5.6 my) well before the volcanic front in central Mexico may be attributed to release of fluid mostly occurring before the slab reaches this distance. The existence of active volcanoes suggests some fluid release which causes partial melting of the mantle-wedge asthenosphere above and results in the volcanic activity. The slab, however, may be too hot (T > 600 ºC; Manea et $al.$, 2004) for brittle rupture and, hence, the lack of seismicity. In this context, the detection of the 2015 intraslab is important as it provides the first evidence from an earthquake that the plate is at a depth of ~ 100 km in central Mexico. It was a normal-faulting earthquake even though the focal mechanism is not well constrained. The seismograms of the 2015 earthquake also provide evidence of high attenuation of shear waves propagating, partially, in the mantle-wedge asthenosphere.

Perhaps the intraslab seismicity beneath active volcanoes in central Mexico at M ~3 level is abundant but has not been documented in the past because of poor instrumentation. New seismic stations in the region should provide high-quality recordings of such events and lead to firm support to the preliminary conclusions reached in this study that are based on the analysis of just one event. Mapping of small intraslab earthquakes below the MVB is important to (1) accurately delineate the geometry of the Benioff zone, (2) understand the likelihood of moderate and large intraslab earthquakes beneath the Mexican Volcanic Belt, (3) estimate ground motions from postulated intraslab earthquakes, and (4) assess impact of intraslab earthquakes on the seismic hazard to cities and town located in the region.

Acknowledgements

References

Brune J.N., 1970, Tectonic stress and the spectra of seismic shear waves from earthquakes. *J. Geophys*. Res., 75, 4997-5009.

García D., Singh S.K., Herraiz M., Pacheco J.F., Ordaz M., 2004, Inslab earthquakes of Central Mexico: Q, source spectra, and stress drop. *Bull. Seism. Soc. Am.*, 94, 789-802.

Ferrari L., Orozco-Esquivel T., Manea V., Manea M., 2012, The dynamic history of the Trans-Mexican Volcanic Belt and the Mexico subduction zone. *Tectonophysics*, 522, 122-149.

Hacker H.R., Peacock S.M, Abers G.A., Holloway S.D., 2003, Subduction factory 2. Are intermediate depth earthquakes in subducting slabs linked to metamorphic dehydration reactions? *J. Geophys.* Res., 108, 2030. https://doi.org/10.1029/2001JB001129

Hjörleifsdóttir V., Singh S.K., Husker A., 2016, Differences in epicentral location of Mexican earthquakes between local and global catalogs: an update. *Geofísica Internacional*, 55, 79-93.

Kirby S.H., Engdahl E.R., Denlinger R., 1996, Intermediate intraslab earthquakes and arc volcanism as physical expressions of crustal and upper mantle metamorphism in subducting plates, in *Subduction: Top to Bottom, Geophysical Monograph 96*, Bebout G., Scholl D., Kirby S. (Editors), American Geophysical Union, Washington, D.C., 195-214.

Manea V.C., Manea M., Kostoglodov V., Currie C.A., Sewell G., 2004, Thermal structure, coupling and metamorphism in the Mexican subduction zone beneath Guerrero. *Geophys. J.* Int., 158, 775-784. https://doi.org/10.1111/j.1365-246X.2004.02325x

Pacheco J.F., Singh S.K., 2010, Seismicity and state of stress in Guerrero segment of the Mexican subduction zone. *J. Geophys. Res.*, 115(B1). https://doi.org/10.1029/2009JB006453

Pardo, M., Suárez, G., 1995, Shape of the subducted Rivera and Cocos plates in southern Mexico: Seismic and tectonic implications. *J. Geophys. Res.*, 100, 12,357-12,373.

Pérez-Campos X., Espíndola V.H., Pérez J., Estrada J.A., Cárdenas Monroy C., Bello D., González-López A., González Ávila D., Contreras Ruiz Esparza M.G., Maldonado R., Tan Y., Rodríguez Rasilla I., Vela Rosas M.A., Cruz J.L., Cárdenas A., Navarro Estrada F., Hurtado A., Mendoza Carvajal A.J., Montoya-Quintanar E., Pérez-Velázquez M.A., 2018, The Mexican national seismological service: An overview. *Seismol. Res. Lett.*, 89(2A), 318-323. https://doi.org/10.1785/0220170186

Pérez-Campos X., Kim Y.H., Husker A., Davis P.M., Clayton R.W., Iglesias A., Pacheco J.F., Singh S.K., Manea V.C., Gurnis M., 2008, Horizontal subduction and truncation of the Cocos plate beneath central Mexico. *Geophys. Res. Lett.*, 35, L18303. https://doi.org/10.1029/2008GL035127

Quintanar L., Cárdenas-Ramírez A., Bello-Segura D.I., Espíndola V.H., Pérez-Santana J.A., Cárdenas-Monroy C., Carmona-Gallegos A.L., Rodríguez-Rasilla I., 2018, A seismic network for the Valley of Mexico: Present status and perspectives. *Seism. Res. Lett.*, 89(2A), 356-362. https://doi.org/10.1785/0220170198

Shapiro N.M., Singh S.K., Iglesias-Mendoza A., Cruz-Atienza V.M., Pacheco J.F., 2000, Evidence of low Q below Popocateptl volcano and its implications to seismic hazard in Mexico City. *Geophys. Res. Lett.*, 27, 2753-2756.

Singh S.K., Lermo J., 1985, Mislocations of Mexican earthquakes as reported in international bulletins. *Geofísica Internacional*, 24, 333-351.

Singh S.K., Ordaz M., Dattatrayam R.S., Gupta H.K., 1999, A spectral analysis of the May 21, 1997, Jabalpur, India earthquake (M_w=5.8) and estimation of ground motion from future earthquakes in the Indian shield region. *Bull. Seism. Soc. Am.*, 89,1620-1630.

Singh S.K., Pacheco J.F., García D., Iglesias A., 2006, An estimate of shear-wave Q of the mantle wedge in Mexico. *Bull. Seism. Soc. Am.*, 96, 176-187.

Singh S.K., Reinoso E., Arroyo D., Ordaz M., Cruz-Atienza V., Pérez-Campos X., Iglesias A., Hjörleifsdóttir V., 2018, Deadly intraslab Mexico earthquake of 19 September 2017 (M_w7.1): Ground motion and damage pattern in Mexico City. *Seism. Res. Lett.*, submitted.

Song T.R.A., Helmberger D.V., Brudzinski M.R., Clayton R.W., Davis P., Pérez-Campos X., Singh S.K., 2009, Subducting slab ultra-slow velocity layer coincident with silent earthquakes in southern Mexico. *Science*, 324, 502-506.

SSN (2018): Servicio Sismológico Nacional, Instituto de Geofísica, Universidad Nacional Autónoma de México, México. URL: http://www.ssn.unam.mx. doi: https://doi.org/10.21766/SSNMX/SN/MX

Takanami T., Selwyn Sacks I., Hasegawa A., 2000, Attenuation structure beneath the volcanic front in northeastern Japan from broad-band seismograms. *Phys. Earth Planet. Interiors*, 121, 339-357.

Tsumura N., Matsumoto S., Horiuchi S., Hasegawa A., 2000, Three-dimensional attenuation structure beneath the northeastern Japan arc estimated from spectra of small earthquakes. *Tectonophysics*, 319, 241-260.

A Probabilistic Model to Quantify the Quality of Open Water Bodies

Jorge Lira

Resumen

Se desarrolló un modelo para cuantificar la calidad de los cuerpos de agua abiertos sobre la base de la lógica probabilística multivariada. El modelo se basa en parámetros de calidad del agua que ya habían sido reportados en la literatura, tales como: turbidez, clorofila-a, índice de vegetación y usos de la temperatura superficial derivadas de la distribución de valores de píxeles de los parámetros. Dichas funciones se combinaron mediante la lógica probabilística multivariada que produjo un mapa de niveles de calidad del agua. Posteriormente, el modelo se aplicó a los humedales Centla, ubicados en el sureste de México. En ellos pueden observarse numerosos cuerpos de agua en niveles de eutrofización variables. Para probar el modelo propuesto, se desarrollaron ejemplos usando una imagen Terra/Aster. Además, se propuso una escala cualitativa de grados de calidad del agua.

Palabras clave: calidad del agua, lógica probabilística, parámetros del agua, humedales Centla

Abstract

A model to quantify the quality of open water bodies was developed on the grounds of multivariate probabilistic logic. The model is based on water quality parameters reported in the scientific literature such as: turbidity, chlorophyll-a, vegetation index and superficial temperature and uses probabilistic functions derived from the distribution of Pixel values of such parameters. Such functions were combined by means of the multivariate probabilistic logic that produced a map of water quality levels. The model was then applied to the Centla Wetlands in South East Mexico. In these wetlands, numerous water bodies can be observed in varying levels of eutrophication. To test the proposed model, examples were developed using a Terra/Aster image. A qualitative scale of water quality degrees was proposed.

Keywords: Water quality, Probabilistic logic, Water parameters, Centla Wetlands

Jorge Lira*
Instituto de Geofísica
Universidad Nacional Autónoma de México
Av. Universidad 3000
04510 Ciudad de México, México
*Corresponding author:jlira@geofisica.unam.mx

I. Introduction

To define and quantify the quality of open water bodies many researchers in the field of environmental monitoring have utilised a number of parameters. For such quantification of water quality, several satellite-derived parameters were considered (Menken and Brezonik 2006; Philipson *et al.* 2016; Mushtaq and Lala 2017; Masocha *et al.* 2017). Various water quality parameters were derived using an airborne hyperspectral spectrometer (Koponen *et al.* 2002; Mobley *et al.* 2005). The most frequent parameters used are: chlorophyll-a, total suspended particles and transparency (Doña *et al.* 2014; Harvey *et al.* 2015). The transparency is determined by the Secchi disk depth (Song *et al.* 2011) and the suspended particles comprehend dead, inert and degraded organic matter (Reza 2008; Kilham at al. 2012; Yang *et al.* 2017). The transparency is inversely proportional to turbidity, the latter of which is determined by the absorption and scattering of light within a water column (Aguilar-Maldonado *et al.* 2017). The chlorophyll-a concentration is directly related to phytoplankton biomass and is used as an indicator for eutrophication (Menken and Brezonik 2006).

The Organization for Economic Co-operation and Development (OECD) defines eutrophication as the water enrichment in nutritive substances that generally leads to changes such as the increase in algae production and other aquatic plants, and the deterioration of water quality and aquatic ecosystem (Doña et al. 2014). The states of eutrophication are: ultraoligotrophic, oligotrophic, mesotrophic, eutrophic and hypertrophic. The water quality is inversely proportional to the degree of eutrophication. Other water quality parameters, related to bio-chemical and thermodynamic processes in inland waters, were considered using vector regression and neural networks modelling with a limited sampling (Wang et al. 2011). The distribution of superficial temperature was also considered as an indicator of water quality (Korosov et al. 2007). For remote sensing studies of water quality using satellite images, only parameters with an optical response can be considered. A multivariate analysis of temperature, salinity and dissolved oxygen was performed using cluster analysis, principal component analysis and partial least square to assess the water quality of a coastal lagoon (Basatnia et al. 2018). The results indicated the critical need to monitor coastal water on a regular basis.

To retrieve water quality parameters from a multispectral satellite image, four different methods were applied (Campbell *et al.* 2011; Gholizadeh *et al.* 2016): (i) the look up table approach that compares the measured spectra response of optical water constituents with stored spectra; (ii) the neural network method that compares a large number of training data spectra to the measured spectra (Pozdnyakov *et al.* 2005a; El Din *et al.* 2017); (iii) the emPirical-regression that relates a linear combination of image bands with in-situ measurements (Bilge *et al.* 2003; Ficek *et al.* 2011; Lessels and Bishop 2013; Doña *et al.* 2014; Bonansea *et al.* 2015); (iv) the inversion/optimization method to simulate the spectra from a set of parameters that minimizes a cost function (Campbell *et al.* 2011). All four methods require a multispectral satellite image with adequate spatial and temporal resolution and in-situ measurements gathered close in time to the date of image acquisition.

A review article that accounts for space borne and airborne sensors used in the assessment of water quality was published in the scientific literature (Gholizadeh *et al.* 2016). The authors of the review included a comprehensive discussion of sensors and methods used in the evaluation of water quality parameters.

The research published accounts for the spatial and temporal variations of water quality parameters. However, a model that combines such parameters to produce a single output map dePicting varying levels of water quality is still required.

In this research a probabilistic model combining several water quality parameters is proposed. The water quality parameters considered are: Turbidity, Chlorophyll-a, Vegetation Index and Superficial Temperature. A model that considers such parameters and
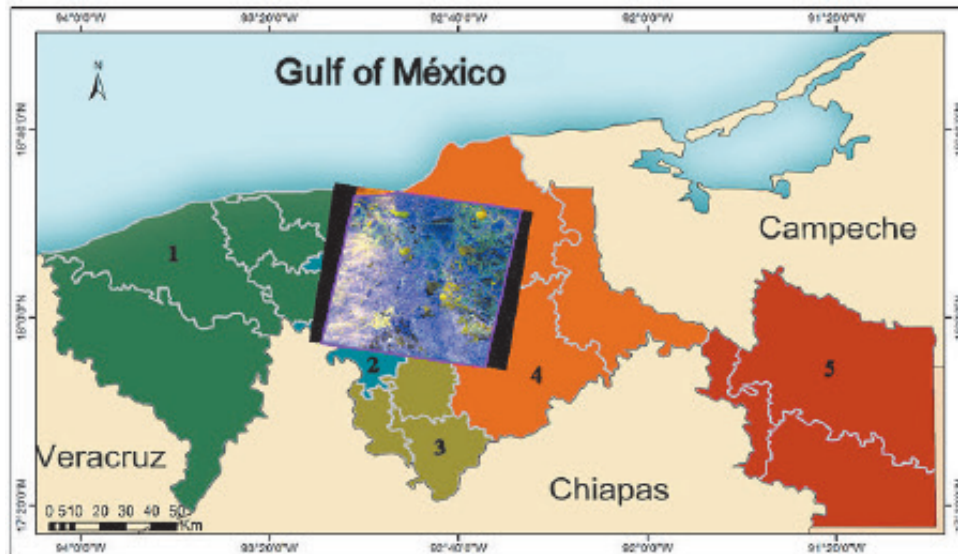
Figure 1. Area of study in Tabasco State, Southeast Mexico

produces a single image dePicting the degree of water quality is required. The model reported in this research combines such parameters using a procedure, based on fuzzy logic, and derived from multivariate probabilistic logic (Nilsson, 1986; Adams, 1996; Zalta *et al.* 2019). Multivariate probabilistic logic has been used in the past to produce maps of primary productivity (Lira *et al.*, 1992). An algorithm based on fuzzy logic was used to perform a multivariate fuzzy cluster analysis of open water bodies. Three clusters were obtained that represent three levels of water pollution (Wang and Wang 2009). These authors used hierarchical cluster analysis based on fuzzy

cluster and multivariate statistical techniques. Such statistical techniques did not consider a multivariate probabilistic analysis. Rather, the authors employed sampling of water bodies to perform a classification of three levels of water pollution.

Details on the calculation of parameters are provided. A description of the basic principles of multivariate probabilistic logic and its application to model water quality are given. The area of study is the Centla Wetlands located in South East Mexico where numerous water bodies in varying degrees of eutrophication are observed

Table 1. Geophysical details of the subregions of Tabasco (location of the Centla Wetlands).

Subregion	Area (Ha)	Precipitation (mm)	Average height (masl)
Chontalpa	746,289	1,225	13.8
Centre	259,380	1,882	7.7
Sierra	184,727	3,711	24.7
Wetlands	663,568	1,225	1.7
Rivers	603,408	2,343	17.0

Ha - Hectares.   masl - Metres above sea level
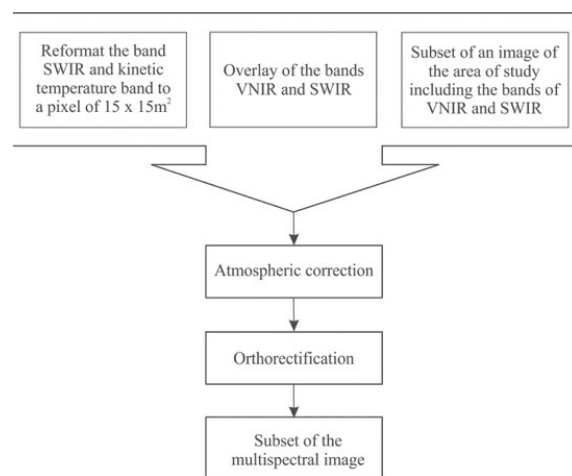
Figure 2. Block diagram of the preprocessing of the Terra/Aster image.

Table 2. Basic characteristics of the Terra/Aster multispectral image

Sensor	Date	Pixel size	Bands (□m)	Image size (pixels)
Terra/ Aster	March 13, 2001	Resampled to 15 x 15 m²	1) [0.52-0.60] 2) [0.63-0.69] 3) [0.76-0.86] 4) [1.60-1.70] 5) [2.145-2.185] 6) [2.185-2.225] 7) [2.235-2.285] 8) [2.295-2.365] 9) [2.360-2.430]	2,838 x 4,048

(Guerra-Martinez and Ochoa-Gaona 2006). An example is provided and a discussion of results is included.

II Materials and Methods
II.1 Materials

A wetland is a natural system defined as an extension of salt marshes, marshes, covered with water, regime natural or artificial, permanent or temporary, suspended or current, sweet or salty surfaces (Fondriest 2016). One important characteristic of the wetlands is that the substrate is periodically saturated or covered with water. Such saturation sustains the development of the ground and the communities of plants and animals that inhabit the wetlands.

The Centla Wetlands are located in the State of Tabasco to the South East of Mexico (Figure 1). The State of Tabasco is divided into five subregions: (1) Chontalpa, (2) Center, (3) Sierra, (4) Wetlands, (5) Rivers (Rodriguez 2002; Guerra-Martinez and Ochoa-Gaona 2006). The Centla Wetlands are included in the subregions (2) and (3) (Figure 1). The area covered by the satellite image is appreciated in Figure 1. Such image was overlaid over the subregions. Such overlay hinders the boundaries of the subregions. If such boundaries were shown in figure 1, the Centla water bodies would not be appreciated in its full extent.

A detailed description of the open water bodies that form the Centla Wetlands is included in the work by Rodriguez (2002). General

morphologic and hydrologic conditions of the water bodies are included in such description. Table 1 provides basic geophysical details about the subregions. To develop the model proposed in this research, a Terra/Aster image was acquired (Table 2 and Figure 1).

II.2 Methods
II.2.1 Preprocessing of Terra/Aster Image

Bands 1 - 9 of the Terra/Aster image were resampled to a Pixel of 15 x 15 m², and geocoded to a UTM projection using the ephemeredes of the Terra/Aster Satellite (Table 2). An atmospheric correction was carried out using
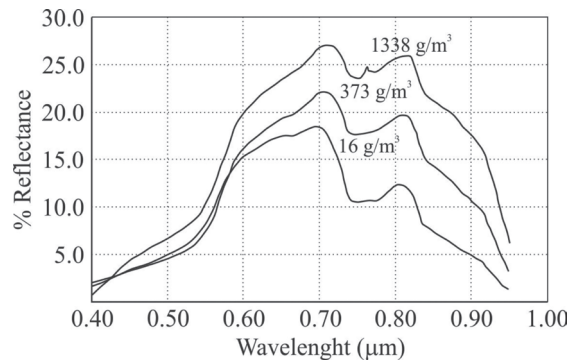
Figure 3. The reflectance of radiation as a function of the wavelength for several concentrations of suspended particles
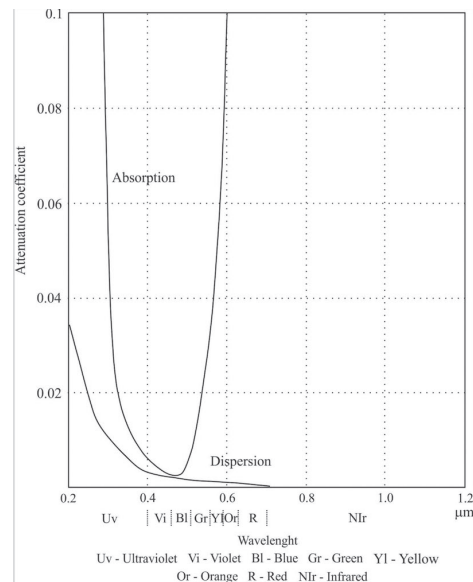
Figure 4. Attenuation of radiation as a result of scattering and absorption of radiation by suspended particles.
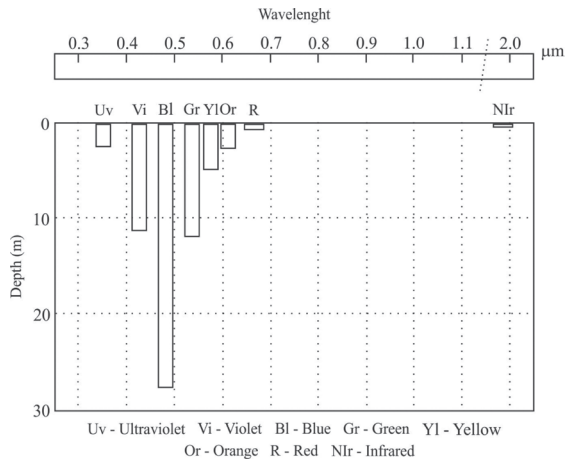
Figure 5. Depth of penetration of radiation as a function of wavelength in the optical region.

the method of dark object subtraction (Chavez 1996). A subimage was extracted to cover the area of the Centla Wetlands. The water bodies were segmented using a previous developed method (Lira 2006). The block diagram of Figure 2 dePicts the preprocessing of the image. The atmospheric correction was applied to the Visible and Near Infrared bands (VNIR) (bands 1-3) and Short Wave Infrared bands (SWIR) (bands 4-9) (Table 2). The kinetic band for the derivation of superficial temperature was acquired with atmospheric correction. The acquisition date of the Terra/Aster image is in line with field data reported by Rodriguez (2002).

II.2.2 Water Quality Parameters

The notion of water quality is used to describe the condition of a water body. This includes the chemical, physical and biological characteristics to quantify the degree to which water is useful with respect to its suitability for a particular purpose (Bartran and Ballance 1996). In this research the purpose is to determine the degree to which water is clean. Therefore, the parameters selected to quantify water quality of the water bodies in the study area are: Turbidity, Chlorophyll-a, Vegetation Index, and Temperature. These parameters were selected on the grounds of methods and results published in the scientific literature. The rational and calculation of these parameters is provided in the following sections.
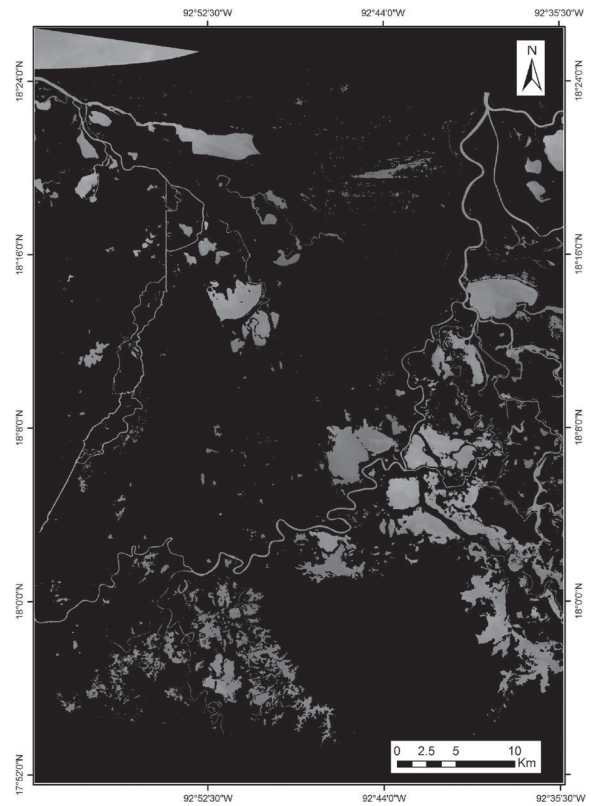
Figure 6. Turbidity map of the area of study.
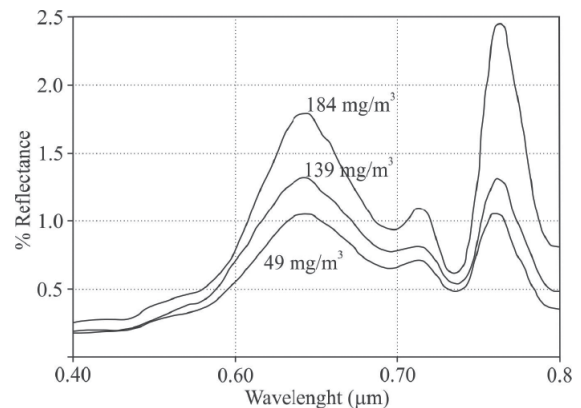
Figure 7. Spectra of Chlorophyll-a for several concentrations of this pigment.

Turbidity

The turbidity is used as a unit of measure to quantify the transmission of radiation through a column of water. Turbidity is defined as the degree of the haziness in water caused by suspended solids. The radiation is scattered and absorbed by the presence of suspended
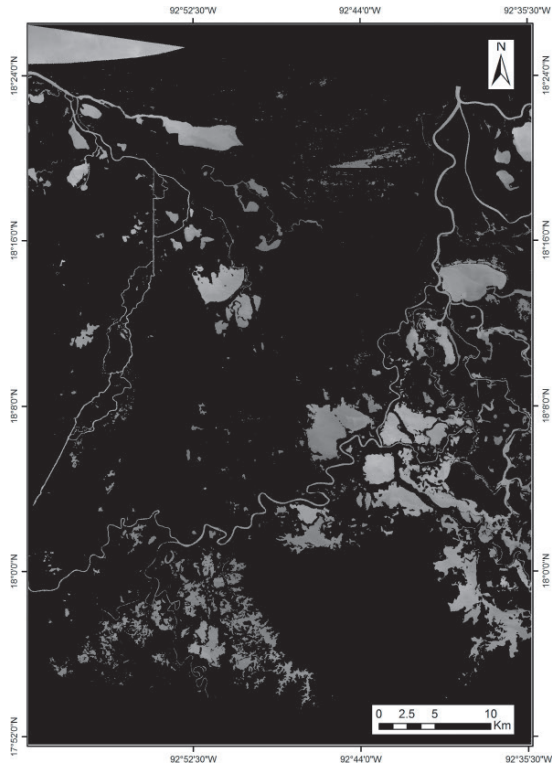
Figure 8. Chlorophyll-a map of the area of study.
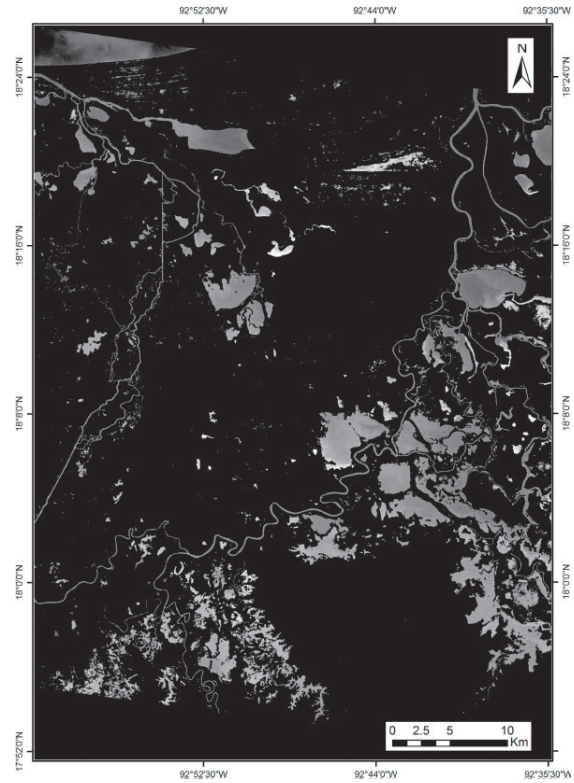
Figure 9. Vegetation index map of the area of study.

organic and inorganic particles in the water. The scattering of radiation increases as the density of suspended particles becomes higher (Roberts *et al.*, 1995) (Figure 3). The emPirical algorithms are derived from transfer radiation models that consider the spectral characteristics of suspended particles in the water (Ritchie *et al.* 2003). The scattering and absorption of radiation by suspended particles is a function of the wavelength (Bukata *et al.*, 1995) (Figure 4). The depth of penetration of radiation is a function of the wavelength (Bukata *et al.*, 1995) (Figure 5). The water bodies of the Centla Wetlands belong to Case II of inland waters (Pozdnyakov *et al.* 2005b). For this case, the model selected is

$$\text{Turbidity} = \frac{\text{Band1}/\text{Band2}}{\text{Band3}/\text{Band2}} \qquad (1)$$

The histogram of the image produced by equation (1) was elongated to a range of [0,255]. Figure 6 shows the Turbidity for the area of study.
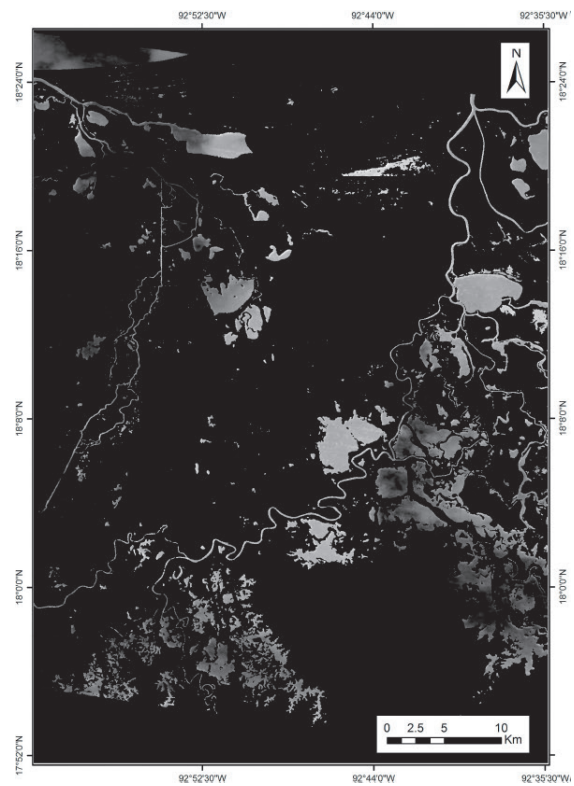
Figure 10. Superficial temperature map of the area of study.

Chlorophyll-a

The Chlorophyll-a is a photosynthetic Pigment. The concentration of Chlorophyll-a provides an indication of the volume of aquatic plants present in a water column. This Pigment is present in all groups of algae in coastal water bodies. The spectra for several concentrations of Chlorophyll-a shows a low reflectance in the bands corresponding to blue and red (Menken *et al.*, 2006) (Figure 7). Instead, in the bands of green and near infrared, a high reflectance is observed (Figure 7). On the grounds of the behaviour of such spectra (Doña *et al.*, 2014; Bonansea *et al.*, 2015), the model to calculate Chlorophyll-a is then

$$\text{Chlorophyll-a} = \frac{\text{Band}\,1}{\text{Band}\,2} \qquad (2)$$

The histogram of the image produced by equation (2) was elongated to a range of [0,255]. Figure 8 shows the Chlorophyll-a for the area of study.

Vegetation Index

Algae are plants that may affect water quality adversely by lowering the dissolved oxygen in the water. Some species of macrophytes in wetland areas can be detected by remote sensing. Species such as hydrilla and salvinia can be found in the area of study. In particular, salvinia is a floating plant in warm water bodies. The raPid growth rate of such plants can lead to a decrease in oxygen concentrations. The NDVI is used to estimate the presence of floating vegetation in the water bodies. The NDVI is defined as

$$\text{NDVI} = \frac{\text{Band}\,3 - \text{Band}\,2}{\text{Band}\,3 + \text{Band}\,2} \qquad (3)$$

The histogram of the image produced by equation (3) was elongated to a range of [0,255]. Figure 9 shows the Vegetation Index for the area of study.

Superficial Temperature

Temperature may be defined as a measurement of the average thermal energy of a substance. The solubility of oxygen and other gases will decrease as temperature increases. Therefore, an increase in temperature brings a decrease in water quality. The image of kinetic temperature was acquired from LP DAAC (Land Processes Distributed Active Archive Center) of NASA (National Aeronautics and Space Administration). This temperature image was generated from the five thermal bands (TIR); its original dimensions were 700 x 830 Pixels with a Pixel of 90 x 90 m². A reformat was applied to generate an image of the same size as the VNIR bands with a Pixel of 15 x 15 m². On the grounds of Planck law, the temperature emissivity algorithm was applied to the TIR bands. Such bands were previously corrected by atmospheric effects. The histogram of the image produced by the emissivity algorithm was elongated to a range of [0,255]. Figure 10 shows the Superficial Temperature for the area of study.

II.2.3 Multivariate Probabilistic Model

Nilsson (1986) first used the term probabilistic logic, where the truth-values of sentences are probabilities. The proposed semantical generalization induces a probabilistic logical entailment or logical consequence. If the probabilities of the argument premises are

Table 3. Matrix correlation among water quality indicators

	Chlorophyll-a	NDVI	Temperature	Turibidity
Chlorophyll-a	1.0000	-0.13327	-0.28643	0.74188
NDVI	-0.13327	1.0000	-0.28030	-0.38962
Temperature	-0.28643	0.28030	1.0000	-0.30620
Turbidity	0.74189	-0.38962	-0.30620	1.0000
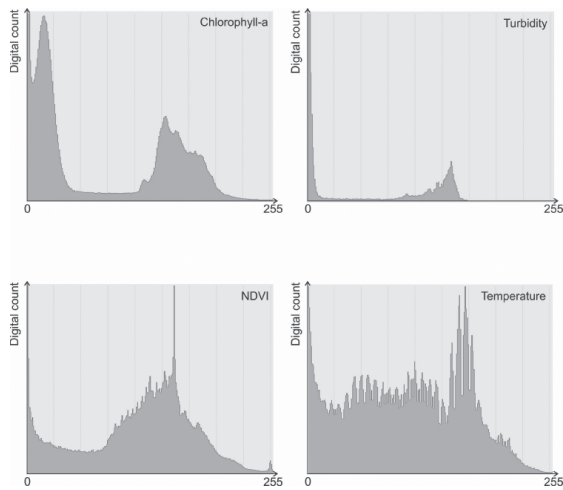
Figure 11. Histograms of the indicators used in the model of water quality.

Parameter Pi	Implication	Natural Processes Q
Turbidity	Increases	Water quality decreases
Chlorophyll-a	Increases	Water quality decreases
Vegetation index	Increases	Water quality decreases
Superficial temperature	Increases	Water quality decreases

known, then the probability of its conclusion may be derived (Adams 1996; Zalta *et al.* 2019). In this sense, the multivariate probabilistic model is based on the fact that probability functions can be assigned to logical sentences such as

$$P1 ==> Q, P2 ==> Q, . . ., Pn ==> Q \qquad (4)$$

These sentences read as follows: if indicator *Pi* exists, the natural process Q exists with a certain probability. Such probability is given by the density functions derived from indicator *Pi*. The implication *Pi ==>* Q, is a fuzzy set. If the value of the indicator *Pi* changes, the probability of the state of the natural process Q changes as well. In he multivariate probabilistic theory, the variables *Pi* are named indicators. In this research, the variables *Pi* are identified as the parameters described in Section II.2.2. The natural process Q is identified as the water quality. In the scientific literature, the physical quantities: Turbidity, Chlorophyll-a, NDVI and Superficial temperature are considered as parameters. The water quality is the variable that depends upon such parameters.

In an image, the value of indicator *Pi*, varies from one location to another, i.e., from Pixel to Pixel. A Pixel, defined as an elementary cell (k,l), implies that the logic sentence *Pi ==>* Q, is extended to every cell (k,l) where these are the coordinates of a Pixel in the image of a parameter.

Due to the fuzziness of the sentence *Pi ==>* Q, there is some degree of redundancy among indicators (Table 3). The correlation matrix (Table 3) indicates low correlation among the indicators. Therefore, the probability of the occurrence of Q should be evaluated when its
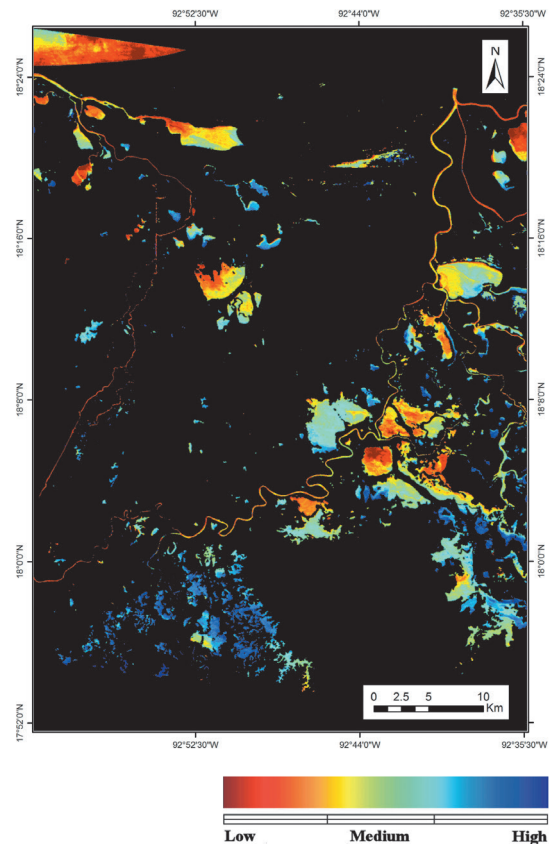
Figure 11. Thematic map of water quality in the area of study.

corresponding indicators occur simultaneously. For such evaluation we consider the intersection of every set determined by various indicators as

$$(P1 \cap P2 \cap P3 \cap ...Pn) ==> Q, \text{for every cell } (k,l) \quad (5)$$

The logical interpretation of this sentence is: if all indicators Pi occur simultaneously, the process Q can be calculated with some degree of probability. Equation (5) may be rewritten as

$$\bigcap_{i=1}^{n}(Pi \Rightarrow Q) \quad \text{, for every cell } (k,l) \quad (6)$$

Expression (6) is written explicitly as (Adams 1996; Zalta *et al.* 2019; Doménech et al, 2017)

$$1 - [-P1 \rightarrow Q)][1 - P2 \rightarrow Q)]...[1 - Pn \rightarrow Q)] = \bigcap_{i=1}^{n}(Pi \Rightarrow Q) \quad (7)$$

Since $Pi ==> Q$ are sets, equation (7) is equivalent to

$$\mathcal{P} = 1 - \prod_{i=1}^{n}(1 - Pi) \text{ , for every cell } (k,1) \quad (8)$$

The right term of equation (7) is the probability P of the occurrence of the process Q.

Since expression (8) is valid for every cell (k,l), the result is a spatial distribution of P. The result of P is an image where the probability of occurrence of Q is dePicted. The model (Expression 8) is dependent on the probability functions associated to the logic sentence $Pi ==> Q$. These functions must be modelled analytically or as tables supported by geophysical and biochemical principles and field data (Lira *et al.* 1992). In this research the probability functions are chosen as the density function associated to the Pixel values of each indicator. The histogram of the image parameters is a good approximation of the density functions (Figure 11). Since the histograms of image parameters are in the range [0,255], equation (8) is written as

$$\mathcal{P} = 255 - \prod_{i=1}^{n}(255 - Pi) \text{ , for every cell } (k,1) \quad (9)$$

The implication is that $Pi ==> Q$ may have a direct or an inverse relationship. In this research an inverse relationship was determined. On the grounds of the discussion of Section II.2.2, the following set of implications describes the relationship of the parameters selected and the state of the natural processes Q.

In brief: if Pi increases $==>$ Q decreases.

Equation (9) was applied to the parameters selected in this research and the results are shown in Figure 12. The result of equation (9) is a map dePicted as an image in figure 12. The digital values of such image were assigned colors using a linear function. The color scale at the bottom of figure 12 is the visual representation of the relation digital value $\leftrightarrow$ color.

III. Results and Discussion

The four parameters calculated in this research for the generation of a water quality thematic map are dePicted in: figure 6 - Turbidity, figure 8 - Chlorophyll-a, figure 9 - Vegetation index, figure 10 - Superficial temperature. The histograms of indicators are in figure 11. The thematic map is shown in figure 12 and the discussion is divided according to such parameters. On the grounds of the definition of water quality used in this research (Bartran and Ballance 1996; Fondriest 2016), a qualitative colour code was associated to the thematic map. Such colour code dePicts the degree of water quality in the area of study of this research.

Turbidity

The North-West corner of the turbidity image shows a portion of the Gulf of Mexico. Due to the high concentration of sediments in the near-shore of the ocean, the turbidity is high (Figure 6). The water bodies with a connection to the ocean show a high level of turbidity as well. The rivers and canals located to the West and East show a high turbidity. A group of water bodies located to the Centre-East of the image has a high turbidity, whereas the water bodies to the South and Southeast are dePicted with low turbidity.

Chlorophyll-a

The Chlorophyll-a is high in the water bodies located to the Centre-East and Centre-South of the image (Figure 8). A high value is also observed in the near-shore ocean. An elongated body connected to the ocean shows a gradient of values for the whole set of parameters. A body in the centre of the image shows a high level of Chlorophyll-a. Other bodies located to the South-West show high values as well.

Vegetation index

Small bodies in the Centre-North and South-West are dePicted with high values of the vegetation index (Figure 9), while medium values are observed in the bodies to the South. The bodies connected to a river and to the ocean have a low value. Rivers and canals are observed with medium values. The near-shore ocean shows the lowest value.

Superficial temperature

The superficial temperature shows moderate values for medium size water bodies isolated from rivers or canals (Figure 10). The two large bodies located at the centre of the image appear as high temperature. A group of small bodies to the Centre-North have high temperature as well. The elongated body to the North, with connection to the ocean, appears with a gradient of temperature.

Thematic map

Figure 12 shows the thematic map derived from the model proposed in this research. A qualitative colour scale is included to indicate the levels of water quality. In general, isolated small water bodies have an appearance of high quality. The water bodies located to the South show medium and high quality, and the near-shore ocean and the water bodies connected to the sea appear with low water quality. Several bodies are dePicted with a gradient of water quality.

IV. Conclusions

Four parameters related to water quality published in the scientific literature, were calculated using a Terra/Aster image that includes the thermal band. The parameters were obtained on the grounds of well-known algorithms reported in several instances in the scientific literature. Such parameters were used in a multivariate probabilistic model to produce a thematic map of water quality for open water bodies. At present, water quality has been determined on the grounds of one parameter or several parameters but taken separately. The model suggested in this research, considers the joint use of the four most frequently reported parameters for water quality. A map is derived using equation (9). However, no quantitative scale yet has been defined. More work is required in this sense.

At present, no joint use of such parameters has been reported in the literature and no quantitative scale of water quality has been defined. The term water quality is usually employed with respect to its suitability for a particular purpose. In this research water quality is understood as the degree to which water is clean. A water is clean when it served the purpose of human consumption. Human consumption is understood in this work as water suitable for drinking ingestion and agricultural use. Thus, a high quality water body as derived in the present research may be considered as water adequate for human consumption. Therefore, a qualitative scale was associated to the colour-levels indicated in the water quality thematic map. Most of the water bodies show a gradient and a complex pattern of water quality. The water bodies to the South and Southeast exhibit a uniform degree of high water quality. All isolated water bodies appear with high values of water quality. The lowest quality observed was in the bodies that have some sort of connection to rivers and the ocean.

The map shown in figure 12 may be used to determine potential uses of the water for human consumption or agriculture. A good quality of the water is the most important asset to decision makers as discussed in the introduction.

A possible area of application of the model developed in this research may be the complex of lagoons in the area of TamPico-Altamira. The water of such lagoons is employed for human consumption; a critical decision must be made in this regard.

V. References

Adams, E.W., 1996. A primer of probability logic, CSLI Publication.

Aguilar-Maldonado, J.A., Santamaría-del-Ángel, E, Sebastiá-Frasquet. M.T.,2017, Reflectances of SPOT multispectral images associated with the turbidity of the Upper Gulf of California. *Revista de Teledección*, 50, 1 - 16.

Bartran J., Ballance R., 1996, Water quality monitoring - A practical guide to the design and implementation of freshwater quality studies and monitoring programmes. United Nations Environment Programme and the World Health Organization, Chapter 2, Water Quality.

Basatnia N., Hossein, S.A, Rodrigo-Comino J, Khaledian Y, Brevik E.C., Aitkenhead-Peterson J., Natesan U. , 2018, Assessment of temporal and spatial water quality in international Gomishan Lagoon, Iran, using multivariate analysis. *Environmental Monitoring and Assessment*, 19:314. /doi.org/10.1007/s10661-018-6679-2.

Bilge F, Yazici B, Dogeroglu T., Ayday C., 2003, Statistical evaluation of remotely sensed data for water quality monitoring. International Journal of Remote Sensing, 24, 5317 - 5326.

Bonansea M., Rodriguez M.C., Pinotti L., Ferrero S., 2015, Using multi-temporal Landsat imagery and linear mixing models for assessing water quality parameters in Río Tercero reservoir (Argentina). *Remote Sensing of Environment*, 158, 28 - 41.

Bukata R., Jerome J.H., Kondratyev K.Y., Pozdnyakov D.V., 1995, Optical properties and remote sensing of inland and coastal waters, New Cork: CRC Press.

Campbell G., Phinn S.R., Dekker A.G., Brando V.E., 2011, Remote sensing of water quality in an Australian troPical freshwater impoundment using matrix inversion and MERIS images. Remote Sensing of Environment, 115, 2402 - 2414.

Chavez Jr., P.S. ,1996, Image-based atmospheric corrections - Revisited and improved. Photogrammetric Engineering and Remote Sensing, 62, 1025–1036.

Doménech J.L.U., Nescolarde-Selva J.A., Segura-Abad L., 2017, Dialectical multivalued logic and probabilistic theory. Mathematics, 5, 15, doi:10.3390/math5010015.

Doña C., Sánchez J.M., Caselles V., Dominguez J.A., Camacho A., 2014 EmPirical relationships for monitoring water quality of lakes and reservoirs through multispectral images. IEEE Journal of Selected ToPics in Applied Earth Observations and Remote Sensing, 7, 632 - 1641.

El Din E.S., Zhang Y., Suliman A., 2017, MapPing concentrations of surface water quality parameters using a novel remote sensing and artificial intelligence framework. International Journal of Remote Sensing, 38, 1023 - 142.

Ficek D., Zapadka T., Dera J., 2011 Remote Sensing reflectance of Pomeranian Lakes and Baltic. Oceanología, 53, 959 - 970.

Fondriest Environmental, Inc., 2016, Fundamentals of Environmental Monitoring, Water quality. https://www.fondriest.com/environmental-measurements/parameters/water-quality/

Gholizadeh M.H., Melesse A.M., Reddi L., 2016, Spaceborne and airborne in water quality assessment. International Journal of Remote Sensing, 37, 3143 - 3180.

Guerra-Martinez V., Ochoa-Gaona S., 2006, Forest and land use assessment from 1990 to the year 2000 in Pantanos de Centla Biosphere Reserve, Tabasco, Mexico. Investigaciones Geográficas, Boletín del Instituto de Geografía, UNAM, 59, 7 - 25.

Harvey E.T., Kratzer S., Philipson P., 2015, Satellite-based quality monitoring for improved spatial and temporal retrieval of chlorophyll-a in coastal waters. Remote Sensing of Environment, 158, 417 - 430.

Kilham, N.E., Roberts D., Singer M.B., 2012, Remote sensing of suspended sediment concentrations during turbid flood conditions of the Feather River, California - A modeling approach. Water Resources Research, 48, W01521. doi:10.1029/2011WR010391

Koponen S., Pulliainen J., Kallio K., Hallikainen M., 2002, Lake water quality classification with airborne hyperspectral spectrometer and simulated MERIS data. Remote Sensing of Environment, 79, 51 -59.

Korosov A.A., Pozdnyakov D.V., Pettersson L.H., Grassl H., 2007, Satellite-data-based study of seasonal and spatial variations of water temperature and water quality parameters in Lake Ladoga. Journal of Applied Remote Sensing, 1, 011508.

Lessels J.S., Bishop T.F.A., 2013, Estimating water quality using linear mixed models with stream discharge and turbidity. Journal of Hydrology, 498, 13 - 22.

Lira, J., Marzolf, G.R., Marocchi, A., Naugle B., 1992, A probabilistic model to study spatial variations of primary productivity in river impoundments. Ecological Applications, 2, 86 - 94.

Lira J., 2006, Segmentation and morphology of open water bodies from multispectral images. International Journal of Remote Sensing, 27, 4015 - 4038.

Masocha M., Dube T., Nhiwatiwa T., Chomura D., 2017, Testing utility of Landsat 8 remote assessment of water quality in two subtroPical African reservoirs with contrasting trophic states. Geocarto International 2017. doi: 10.1080/10106049.2017.1289561.

Menken K.D., Brezonik P.L., 2006, Influence of Chlorophyll and colored dissolved organic matter (CDOM) on lake reflectance spectra: implications for measuring lake properties by remote sensing. Lake and Reservoir Management, 22, 179 - 190.

Mobley C.D., Sundman L.K., Davis C.O., Bowles J.H., Downes T.V., Leathers R.A., Montes M.J., Bissett W.P., Kohler D.D.R., Reid R.P., Louchard E.M., Gleason A., 2005, Interpretation of hyperspectral remote-sensing imagery by spectrum matching and look-up tables. Applied Optics, 44, 3576 - 3592.

Mushtaq F., Lala, M.G.N., 2017, Remote estimation of water quality parameters of Himalaya lake (Kshmir) using Landsat 8 OLI imagery. Geocarto International, 32, 274. 285.

Nilsson, N., 1986, Probabilistic logic. Artificial Intelligence, 28, 71 - 87.

Philipson P., Kratzer S., Mustapha S.B., Strömbeck N., Steler K., 2016, Satellite-based water quality monitoring in Lake Vänern Sweden. International Journal of Remote Sensing, 37, 3939 - 3960.

Pozdnyakov D., Korosov A., Grassl H., Pettersson L., 2005a, An advanced algorithm for operational retrieval of water quality from satellite data in the visible. International Journal of Remote Sensing, 26, 2669 - 2687.

Pozdnyakov D., Shuchman R., Korosov A., Hatt Ch., 2005b, Operational algorithm for the retrieval of water quality in the Great Lakes. Remote Sensing of Environment, 97, 352 - 370.

Reza M.M., 2008, Assessment of suspended sediments concentration in surface waters, using Modis images. American Journal of Applied Sciences, 5, 798 - 804.

Ritchie J., Zimba P., Everitt J., 2003, Remote sensing techniques to assess water quality. Photogrammetric Engineering and Remote Sensing, 69, 695 - 704.

Roberts A., Kirman C., Lesack L., 1995, Suspended sediment concentration estimation from multi-spectral video imagery. International Journal of Remote Sensing, 16, 2439 - 2455.

Rodriguez E., 2002, Las Lagunas Continentales de Tabasco. Universidad Juarez Autónoma de Tabasco, México.

Song K., Wang Z., Blackwell J., Zhang B., Li F., Zhang Y., Guangjia J., 2011, Water quality monitoring using Landsat Thematic Mapper data with emPirical algorithms in Chegan Lake, China. Journal of Applied Remote Sensing, 5, 053506-1 - 053506-16.

Wang, X., Wang, Q., 2009, Evaluation of landscape water bodies using fuzzy cluster and multivariate statistical techniques. Proceedings, IEEE International Conference on Intelligent Computing and Intelligent Systems, 20 - 22 November, 2009, Shangai, China, DOI: 10.1109/ICICISYS.2009.5357640.

Wang X., Fu L., He C., 2011, Applying support vector regression to water quality modeling by remote sensing data. International Journal of Remote Sensing, 23, 8615 - 8627.

Yang X., Sokoletsky L., Wei X., Shen F., 2017, Suspended sediment concentration mapPing based on the Modis satellite imagery in the East China inland, estuarine, and coastal waters. Journal of Oceanology and Limnology, 35, 39 - 60.

Zalta, E.N., Nodelman, U., Allen, C., Anderson, L. (Eds), 2019, Logic and Probability, The Stanford Encyclopedia of Philosophy, Stanford University, Stanford, CA, 94305, USA.

The divide-and-conquer framework: a suitable setting for domain decomposition methods of the future

Ismael Herrera-Revilla, Iván Contreras and Graciela S. Herrera*

Resumen

Este artículo surgió a partir de experimentos numéricos, en los cuales ciertos algoritmos, que en algunos textos científicos (DVS-BDDM) produjeron aceleración (o speedups) muchas veces mayores a la cantidad de procesadores utilizados (existen casos ya abordados de más de setenta, pero probablemente a menudo son mucho mayores). Con base en estos resultados sobresalientes, en este artículo se demuestra que creer en la aceleración ideal estándar, que se considera igual a la cantidad de procesadores, ha sido una limitante en el rendimiento buscado a través de distintas investigaciones sobre métodos de descomposición de dominio (MDD) y hasta el momento ha obstaculizado mucho su desarrollo. Por lo tanto, se propone una teoría mejorada en la que el objetivo de aceleración se base en el paradigma algorítmico "Divide y vencerás", considerado con frecuencia como el leitmotiv de los métodos de descomposición de dominio, como un escenario adecuado para el MDD del futuro.

Palabras clave: MDD, DVS-DDM, computación paralela, aceleración paralela ideal, dividir y vencerás.

Abstract

This paper was prompted by numerical experiments we performed, in which algorithms that Ismael Herrera Research Group previously developed (the DVS-BDDC) and are already available in the literature, yielded accelerations (or, speedups) many times larger (more than seventy in some examples already treated, but probably often much larger) than the number of processors used. Based on such outstanding results, this paper shows that believing that the ideal speedup is equal to the number of processors, has limited the performance-goal sought by researchers on domain decomposition methods (DDM) and has hindered much its development, thus far. Hence, an improved theory in which the *speedup goal* is based on the Divide and Conquer algorithmic paradigm, frequently considered as the leitmotiv of domain decomposition methods, is proposed as a suitable setting for the DDM of the future.

Keywords: DDM, DVS-DDM, parallel computation, ideal parallel speedup, divide and conquer.

I. Herrera-Revilla
Instituto de Geofísica
Universidad Nacional Autónoma de México (UNAM)
Apdo. Postal 22-220, México, D.F. 14000

I. Contreras
Instituto de Geofísica
Universidad Nacional Autónoma de México (UNAM)
Apdo. Postal 22-220, México, D.F. 14000

G. S. Herrera*
Instituto de Geofísica
Universidad Nacional Autónoma de México (UNAM)
Apdo. Postal 22-220, México, D.F. 14000
*Corresponding author: ghz@igeofisica.unam.mx

1. Introduction

The present paper was prompted by some outstanding results that we recently obtained in a sequence of numerical and computational experiments applying some parallel algorithms already available in the literature (the DVS-BDDC [1-8]). They are extraordinary, because contradict the generally accepted belief that in parallel computation the acceleration, or *speedup*, cannot be greater than the processors number [9-22]. For example, in our numerical experiments using 400 processors in parallel we achieve a speedup of 29,278, which is 73.2 times greater than the maximum acceleration that such a belief allows.

In agreement with such a belief, the *speedup goal* sought in most, probably all, research that has been carried out in domain decomposition methods (DDM) up to now [9-20], is equal to the number of processors used. Since our results show that considerably larger speedups are feasible, the conclusion is drawn that the *speedup goal* sought so far is too modest and restrictive; hence, it should be replaced by a larger and more ambitious performance goals in future DDM research. To this end, we resort to the DIVIDE AND CONQUER STRATEGY, which for solving boundary-value problems of PDEs using parallel computation, probably is the most basic algorithmic paradigm [23]. Furthermore, we formulate it in a manner that yields precise and clearly defined quantitative performance goals, to be called DC-goals, which are larger, yet realistic. The adequacy of the modified framework so obtained is verified by satisfactorily incorporating the outstanding results just mentioned in it.

It should be mentioned, before leaving this Section, that according to the Gustafson's Law, the speedup is up-bounded by the number of processors, which is achieved when the linear speedup is attained. However, beyond such limits, the superlinear speedup may happen for plenty of reasons (see [24]), although it is not frequent and when it occurs it enhances the value of the software possessing it.

The paper is organized as follows, Section 2 presents some background material on the Derived-Vector Space (DVS) approach to DDM, and DVS-BDDC [1-8]. The outstanding performance results that prompted this article are introduced and explained in Section 3. An inconsistency of standard approaches to DDM that such results exhibit, is pointed out and discussed in Section 4, while Section 5 introduces some measures of performance whose conspicuous feature is that they are defined with respect to a performance goal.

The ideas and results contained in Sections 3 to 5, are then used in Sections 6 and 7, to show that both, the concept of *ideal parallel-performance* and the belief that the *ideal parallel speedup* is p , lack firm bases. The *"divide and conquer"* algorithmic paradigm ([23], *p. v*), -the *DC-paradigm*- is recalled and revised in Section 8, and a quantitative *DC-performance goal* adequate to be used in future DDM research, is derived from it. There, it is also shown that in the examples here discussed the latter *performance goal* is larger than p , by a big factor; indeed, in the examples here treated, the *DC-speedup goal* is close to p^2 and the factor we are referring to, is close to $p = p^2/p$. We recall that p is the number of processors, used and hence the '*factor*' is large when the number of processors is large.

When the extraordinary numerical and computational results that prompted this paper are incorporated in the *DC-framework* they look completely normal, as it is shown in Section 10, since their *DC-efficiencies*, for $p \neq 1$, range from 70.3% to 20.0%. Sections 11 and 12 are devoted to exhibit the severe restrictions that believing in the relation $S(p,n) \leq p$, has imposed on software developed under that assumption. Finally, Section 13 states this paper's conclusions.

2. Some background

Ismael Herrera and some of his coworkers, have been working in domain decomposition methods (DDM) since 2002, when he organized and hosted the Fourteenth International Conference on Domain Decomposition Methods (DDM) [23]. In their work on DDM [1-8], they pointed out that it is extremely inconvenient using coarse

meshes in which some of the nodes are shared by several subdomains because, when this is done the system matrix is not block-diagonal. This, in turn, shatters one of the main objectives of the DDM strategy: processing in different processors the degrees of freedom belonging to different subdomains of the coarse mesh. So, according to the above discussion, standard methods (i.e., methods that follow the canons prevailing at present) share this handicap and, to overcoming it, we introduced the *derived-vector space* methodology (DVS methodology) [1-8].

The *algebraic venue* in which DVS methodology was built is the *derived-vector space*. Briefly, the *derived-vector space* construction consists in [2]:

i). Firstly, the partial differential equation is discretized by means of a standard procedure in a *fine mesh*. This yields a system of linear discrete equations and a system of *original nodes*. When a coarse mesh is introduced, some of them are shared by several subdomains.

ii). Replacing the *original-nodes by the derived-nodes*. The nodes of this latter class have the property that each one of them belong to one and only one of the subdomains. The whole set of derived-nodes is decomposed into non-overlapping subsets, with the property that there is a one-to-one correspondence between such subsets and sub-domains of the coarse mesh;

iii). Then, the linear-space of functions defined in the *derived-nodes*, constitutes the *derived-vector space*, which is provided with an algebraic structure suitable for effectively carrying out the developments required for constructing the DVS methodology;

iv). The concept of *non-overlapping discretization* is introduced [2]. The most significant and conspicuous property of such a kind of discretizations is that its application yields block-diagonal systems of equations;

v). A *non-overlapping discretization*, equivalent to the standard discretization applied in i), is used. This permit transforming the original system of discrete equations into another whose system-matrix is block-diagonal.

Up to now, the DVS methodology has produced four DVS-algorithms (see, [2] for further details): DVS-FETI-DP, DVS-BDDC, DVS-PRIMAL and DVS-DUAL. The first two were obtained by mimicking the well-known FETI-DP and BDDC procedures in the derived-vector space., but the big and very significant difference is that such procedures are applied after the differential equations have been subjected to a *non-overlapping discretization*, so that the discrete system of linear equations we start with, is block-diagonal. The other two DVS-algorithms: the DVS-PRIMAL and DVS-DUAL, were produced by completing the theoretical framework (again see, [2]). So far, only the DVS-BDDC algorithm has been numerically tested; in 2016, preliminary computational experiments were published, which proved that the DVS-BDDC was fully competitive with the top DDM algorithms that were available [1]. However, at that time we did not have yet obtained the extraordinary results we are now reporting.

Table 1. Results of computational experiments

p	n	$T(p,n)$	$S(p,n)$	$S(p,n)$ in terms of p	$p/S(p,n)$
1	10^6	29,278	1	1p	1
16	10^6	178	164.5	10.28p	.097
25	10^6	78	375.4	15.02p	.067
64	10^6	16	1,829	28.58p	.035
256	10^6	2	14,639	57.18p	.017
400	10^6	1	29,278	73.20p	.014

3. The outstanding results

More recently, in 2018, the authors have developed a more careful code of the DVS-BDDC algorithm and tested it through a set of numerical experiments, obtaining the exceptional results that are presented and discussed in this Section. They are objectively outstanding because, for

example, when the number of processors used is 400 the acceleration produced is 73.2 times by 400; hence, in this application, the DVS-BDDC algorithm produces an acceleration 73.2 times larger than the largest possible according to canonical theory (i.e., theory that follows the canons prevailing at present).

More specifically, the computational experiments here reported, consisted in treating a well posed 2D problem for Laplace differential operator in the highly parallelized supercomputer "Miztli" of the National Autonomous University of Mexico (UNAM), using successively 1, 16, 25, 64, 256 and 400 processors. The notation used to report the numerical and computational results so obtained is given next:

$$Number\ of\ Processors \rightarrow p \qquad (3.1)$$
$$Size\ of\ the\ Problem \rightarrow n$$
$$Execution\ Time \rightarrow T(p,n)$$
$$Speedup \rightarrow S(p,n)$$

Here, the size of the problem is equal to number of degrees of freedom, which in turn is equal to the number of nodes of the fine mesh. In general, the "execution time" and "speedup" are functions of the pair . In the set of numerical experiments here reported the size of the problem is kept fixed and equal to 10^6; i.e., $n=10^6$.

The very impressive results of the numerical experiments are given in Table 1 (everywhere in this paper times are given in seconds), where the fifth column gives the speedup as a multiple of p, the number of processors, which in standard theory of domain decomposition methods is thought to be an unsurmountable *speedup*. However, in the set of experiments we are reporting, the speedup is much greater than the standard theory foresees, if $p \neq 1$; even more, it is greater than such an upper bound, by a large factor: 10.28, 15.02, 28.58, 57.18 and 73.2, when the number of processors is 16, 25, 64, 256 and 400, respectively. Observe that the factor increases with the number of processors, which is an enhancing feature. The last column is only included here, for later use.

4. An inconsistency of standard DDM

The standard definition of efficiency is

$$E_S(p,n) \equiv p^{-1}S(p,n) \qquad (4.1)$$

and it is usually expressed in percentage. The sub-index *S* used here, comes from Standard and it is used for clarity, since alternative definitions will be introduced later.

The Table 2 that follows has been derived from Table 1, by expressing its last column in terms of standard efficiency, $E_S(p,n)$. By inspection of Table 2, where percentages much greater than 100% such as 1,028, 1,502, 2,858, 5,718 and 7,320 occur, it is seen that the standard efficiency is not adequate for expressing the superlinear results of the numerical experiments we are reporting, because efficiencies far beyond 100% occur.

Table 2. Using standard efficiency for expressing our superlinear results

p	n	T(p,n)	S(p,n)	Es (p,n) in percentage
1	10^6	29,278		100%
16	10^6	178	164.5	1,028%
25	10^6	78	375.4	1,502%
64	10^6	16	1,829	2,858%
256	10^6	2	14,639	5,718%
400	10^6	1	29,278	7,320%

5. Revisiting the measures of performance

In this Section we define some measures of parallel-software performance that will be used in the sequel. As usual, such measures will be based on the execution time that is required for completing a task; the shorter the better. According to Eq.(3.1), the notation $T(p,n)$ means the execution time when the number of processors is p; in particular, $T(1,n)$ is the execution time when only one processor is applied.

For the sake of clarity, we recall the *speedup (or, acceleration)* definition:

$$S\left(p,n\right) \equiv \frac{T\left(1,n\right)}{T\left(p,n\right)} \qquad (5.1)$$

The main objective in using a parallel computer is to get a simulation to finish faster than it would in one processor. Furthermore, let us take the position of a software designer who intends to develop software that performs well; so, he defines a *performance goal* he intends to achieve. The following two procedures for specifying such a goal will be considered; fixing the *execution-time goal, $T_G(p,n)$*, or fixing the *speedup goal, $S_G(p,n)$*. Assume either one of them have been specified, then the *relative efficiency* (relative to a goal performance) is defined by

$$E_G\left(p,n\right) \equiv \frac{S\left(p,n\right)}{S_G\left(p,n\right)} \qquad (5.2)$$

when $S_G(p,n)$ is given, or

$$E_G\left(p,n\right) \equiv \frac{T_G\left(p,n\right)}{T\left(p,n\right)} \qquad (5.3)$$

when $T_G(p,n)$ is given.

These two manners of defining *relative efficiency* are equivalent, if and only if:

$$T_G\left(p,n\right)S_G\left(p,n\right) = T\left(1,n\right) \qquad (5.4)$$

Hence

$$S_G\left(p,n\right) = \frac{T\left(1,n\right)}{T_G\left(p,n\right)} \; and \; T_G\left(p,n\right) = \frac{T\left(1,n\right)}{S_G\left(p,n\right)} \quad (5.5)$$

The first one of these equalities can be used to obtain $S_G(p,n)$ when $T_G(p,n)$ is given, and the second one, conversely.

According to Eq.(5.2),

$$E_G\left(p,n\right) = 1 \Leftrightarrow S\left(p,n\right) = S_G\left(p,n\right) \qquad (5.6)$$

Here the symbol $\Leftrightarrow$ stands for the logical equivalence; i.e., if and only if. Actually, when we choose a goal we do not know if it is achievable, but the initial state satisfies $S(p,n)<S_G(p,n)$ since $S_G(p,n)$ is a desirable state. Hence, at the beginning $1-E(p,n)>0$ and this quantity may be taken as a distance to the goal. However, it can also happen that our developments lead to

a speedup $S(p,n)>S_G(p,n)$, since generally we do not know beforehand if the speedup $S_G(p,n)$ is an upper bound of those possible. When that happens, $E(p,n)>1$.

Conversely, a corresponding argument can be made if the execution time and Eq.(5.3) are used to define the parallel efficiency. The main difference is that, in such a case, $T(p,n)>T_G(p,n)$ at the beginning and $T(p,n)<T_G(p,n)$ is an indication that the goal has been exceeded.

6. The concept of "ideal parallel speedup"

In the literature on scientific parallel computing and on domain decomposition methods for the numerical solution for partial differential equations, the notion of "*ideal parallel speedup*" is used when defining absolute efficiency. However, its definition lacks precision. When $S_A(p,n)$ is the *ideal parallel speedup*, the relation

$$S\left(p,n\right) \le S_A\left(p,n\right) \qquad (6.1)$$

holds whenever $S(p,n)$ is the acceleration obtained in a parallel computation. If we try to make this notion rigorous, we could say that $S_A(p,n)$ is the supremum, but what is never made clear is: of what set $S_A(p,n)$ is the supremum.

Even so, when $S_A(p,n)$ is the *ideal parallel speedup, the absolute parallel efficiency* is defined to be

$$E_A\left(p,n\right) \equiv \frac{S\left(p,n\right)}{S_A\left(p,n\right)} \qquad (6.2)$$

Thereby, we mention that the subscript *A* above, comes from *Absolute*.

However, if we do not know for sure that Eq.(6.1) holds whenever $S(p,n)$ is the acceleration obtained in a parallel computation, this is a risky definition. Indeed, if that is the case and there is an execution for which

$$S\left(p,n\right) > S_A\left(p,n\right) \qquad (6.3)$$

Then, we would claim that $S(p,n)$ is not achievable and we would be satisfied with an acceleration that is close to $S_A(p,n)$, even if $S_A(p,n)$ is much smaller than $S(p,n)$.

7. The international DDM research goal

Generally, it is thought that Eq.(6.1) holds, with $S_A(p,n) \equiv p$; i.e.,

$$S(p,n) \le p \qquad (7.1)$$

Hence, the standard definition of efficiency of Eq.(4.1):

$$E_S(p,n) \equiv p^{-1} S(p,n) \qquad (7.2)$$

Comparing this equation with Eq.(5.2) it is seen that Eq.(7.2) implies that the *speedup goal*, sought by DDM research worldwide is:

$$S_S(p,n) \equiv p \qquad (7.3)$$

Here, we have written $S_S(p,n)$ for the *speedup goal* of standard DDM research. In view of the discussions here presented, this goal is too modest and more ambitious goals should be sought in the future.

8. The relative DVS efficiency of standard approaches

In this Section we make a simple exercise in which we compute the *relative efficiency* of standard approaches when the *goal speedup* is that achieved by the DVS-BDDC algorithm in the numerical experiments here reported. The notation here adopted for such a *relative efficiency* is E^S_{DVS}.

Applying the definition of Eq.(5.2), we get

$$E^S_{DVS}(p,n) = \frac{S(p,n)}{S_G(p,n)} \le \frac{p}{S_{DVS}(p,n)} \qquad (8.1)$$

Inspecting the results of our numerical experiments reported in the last column of Table 1, in view of Eq.(7.1), it is seen that the *relative efficiency* of standard approaches with respect to DVS-BDDC is only 9.7%, 6.7%, 3.5%,1.7% and 1.4%, in these experiments. Hence, our conclusion of this Section is that the speedups goals sought in DDM research worldwide up to now, are too small and should be revised.

9. The *Speedup goal* of the Divide and

Conquer Framework

As a starting point of this Section, we recall the **divide and conquer** algorithmic paradigm ([23]), which is frequently considered as the *leitmotiv* of domain decomposition methods [21]. The **divide and conquer strategy** (*DC-strategy*) consists in dividing the domain of definition of the scientific or engineering model into small pieces and then send each one of them to different processors. If p is the number of subdomains of the domain decomposition, the size of each piece is approximately equal to n/p ; hence, smaller than n when $p>1$ and much smaller than n, when p is large.

This is the procedure used by *domain decomposition methods*, for reducing the size of the problems treated by each processor. It constitutes an application of the *DC-strategy*. Of

Table 3. The *DC-execution-time goal* and the *DC-speedup goal*

p	n/p	$T_{DC}(p,n)$	$S_{DC}(p,n)$	p^2	$\{p^2 - S_{DC}(p,n)\}/ p^2$
1	106	29,278	1	1	0%
16	62,500	125.15	233.9	256	8.6%
25	40,000	51.45	596.1	625	4.6%
64	15,625	7.90	3,706	4,096	9.5%
256	4,096	0.55	53,233	65,536	18.8%
400	2,500	0.2	146,390	160,000	8.5%

course, for the **divide and conquer strategy** being most effective it is necessary and sufficient that each one of the *local problems* be independent of all others. Such a condition (each *local problem* being independent of all others) is seldom fulfilled in practice, and it will be referred to as the *DC-paradigm*. Adopting the *DC-paradigm* as a guide in the development of software implies to strive to construct algorithms in which the local problems are as independent of each other as possible. Thereby, we mention that the DVS methodology, which

Table 4. The outstanding results in the DC-framework.

p	p^2	$T_{DVS}(p,n)$	$S_{DVS}(p,n)$	$T_{DC}(p,n)$	$S_{DC}(p,n)$		$SDVS(p,n)/P$
1	1	29,278	1	29,278	1	100%	100%
16	256	178	164.5	125.15	233.9	70.3%	64.3%
25	625	78	375.4	51.45	596.1	63.0%	60.1%
64	4,096	16	1,829	7.90	3,706	49.4%	44.7%
256	65,536	2	14,639	0.55	53,233	27.5%	22.3%
400	160,000	1	29,278	0.2	146,390	20.0%	18.3%

in the numerical experiments here reported has been so effective, was developed following the *DC-paradigm*.

Since the approximate size of each *local problem* is n/p , when all them are independent, $T(1,n/p)$ would be the approximate *execution-time* for each one of them, which when the computation is carried out in parallel is also the global *execution-time.* Therefore, in the *DC-framework* we define the *execution-time goal* (*DC-execution-time goal*), to be denoted by $T_{DC}(p,n)$, as:

$$T_{DC}(p,n) \equiv T(1,n/p) \qquad (9.1)$$

Correspondingly, the *speedup goal* for the DC-approach is defined to be

$$S_{DC}(p,n) \equiv \frac{T(1,n)}{T(1,n/p)} \qquad (9.2)$$

and the *DC-efficiency* is given by

$$E_{DC}(p,n) \equiv \frac{S(p,n)}{S_{DC}(p,n)} = \frac{T(1,n/p)}{T(p,n)} \qquad (9.3)$$

In Table 3, to illustrate the *Divide and Conquer* concepts, they have been computed in the conditions of the numerical experiments that prompted this paper. The first and second columns (counted from left to right) contain the number of processors and the degrees of freedom of the local problems, respectively. The third column yields the DC-execution time goals of the local problems, which were obtained through numerical experiments; for each *p* only one of the local problems was solved numerically (and only one of the processors was used). Once

Table 5. Comparison of *speedup* goals

p	$S_S(p,n)$	$S_{DC}(p,n)$	$S_{DC}(p,n) / S_S(p,n) = S_{DC}(p,n)/p$	$S_{DC}(p,n) / S_{DC}(p,n) = p/ S_{DC}(p,n)$
1	1	1	1	1
16	16	233.9	14.6	.0685
25	25	596.1	23.8	.0420
64	64	3,706	57.9	.0173
256	256	53,233	207.9	.0048
400	400	146,390	365.0	.0027

Table 6. Restrictions of performance for standard software

p	$T_S(p,n) \geq$ $T(1,n)/p$	$S_S(p,n) \leq p$	$T_{DC}(p,n)$	$S_{DC}(p,n)$	$E^S_{DC}(p,n) \leq p/S_{DC}(p,n)$
1	–	–	29,278	1	100%
16	$T_S(16,10^6) \geq$ 1,830	$S_S(16,10^6)$ ≤ 16	125.15	233.9	$E^S_{DC}(16,10^6) \leq 6.85\%$
25	$T_S(25,10^6) \geq$ 1,171.1	$S_S(25,10^6)$ ≤ 25	51.45	596.1	$E^S_{DC}(25,10^6) \leq 4.20\%$
64	$T_S(64,10^6) \geq$ 457.5	$S_S(64,10^6)$ ≤ 64	7.90	3,706	$E^S_{DC}(64,10^6) \leq 1.73\%$
256	$T_S(256,10^6) \geq$ 114.40	$S_S(256,n)$ ≤ 256	0.55	53,233	$E^S_{DC}(256,10^6)$ $\leq 0.48\%$
400	$T_S(400,10^6) \geq$ 73.20	$S_S(400,n) \leq$ 400	0.20	146,390	$E^S_{DC}(400,10^6) \leq$ 0.27%

$T_{DC}(n,p)$ was known, $S_{DC}(p,n)$ was computed applying straightforward formulas. The local solvers used in our numerical experiments were banded *LU* decompositions, whose *algorithmic complexity* turned out to be p^2 and is given in the fifth column. An interesting fact, in the numerical experiments here reported, is that the *algorithmic complexity* approximates $S_{DC}(p,n)$, and the last column of Table 3 gives the corresponding relative errors in percentage associated with such an approximation.

10. Incorporating the outstanding results in the DC–framework

In this Section the results of our numerical and computational experiments contained in Table 1, are incorporated in the DC-framework. Table 4 that follows, was so built. The seventh column of Table 4 gives the DVS efficiency, relative to the Divide and Conquer performance goal. The last column gives it, relative to the complexity of LU, p^2 .

Table 7. Direct comparison of *DC-efficiencies* of standard and DVS-BDDC software

p	16	25	64	256	400
$E_{DC}(p,n)$	70.3%	63.0%	49.4%	27.5%	20.0%
BOUNDS FOR $E^S_{DC}(p,n)$	6.85%	4.20%	1.73%	0.48%	0.27%

By inspection of this table, it is seen that the superlinear results that prompted this paper look perfectly normal when they are displayed in the DC-framework. This shows that the DC-framework is adequate for accommodating the outstanding numerical and computational results that we have obtained using the DVS-BDDC algorithm.

11. Restrictions on parallel performance imposed by the standard framework

Assuming $S(p,n) \leq p = S_S(p,n)$ is limitative and this Section together with the next one we explore more thoroughly the restrictions on parallel performance that such an assumption imposes.

To start with, the *standard speedup goal*, p, and the *DC-speedup goal*, $S_{DC}(p,n)$, corresponding to the set of experiments we have been discussing, are compared. Their ratios are shown Table 5, where the values of $S_{DC}(p,n)$ are taken from Table 4.

By inspection of Table 5, it is seen that the *standard goal-speedups* are much smaller than the *goal-DC-speedups*, and probably too conservative and restrictive.

Table 6, which follows, shows the bounds of performance for any software that satisfies the restriction $S(p,n) \leq p$. The last column of this table shows such an assumption limits severely the *DC-efficiency* that one can hope for, when any of the standard methods is applied, including BDDC and FETI-DP [22].

12. Additional comparisons

To have a clearer appreciation of the relevance of the limitations imposed by the standard framework, which have been established in Section 9, a direct comparison with the results obtained using the DVS-BDDC, which are given in Table 3, can help. Such a comparison is highlighted in Table 7.

In summary, for all the numerical and computational experiments here discussed, the efficiency one can hope to obtain using standard software is only a small fraction of that, which is obtained when the DVS-BDDC algorithm is applied.

From all the above discussion, we draw the conclusion that adopting the definition $S_S(p,n) \equiv p$, as is usually done in domain decomposition methods, is too conservative and hinders drastically the performance of methods developed within such a framework.

13. Conclusions

This paper communicates the outstanding results of numerical experiments in which the DVS-BDDC algorithm [2] yields superlinear speedups, which exceed the number of processors by a large factor; 73.2 is the largest obtained in such experiments. From the results and their analysis here presented, the following conclusions are drawn:

1. The belief that the speedup (or, acceleration) is always less or equal to p (the number of processors) is incorrect. Accelerations much larger than p are not only feasible, but have been achieved using the DVS-BDDC algorithm;

2. The *performance goal* that research on DDM has intended up to now, besides being too small, has been very restrictive for the software developed in that framework; and

3. The *Divide and Conquer framework* here introduced is, by far, more adequate for accommodating the superlinear behavior of domain decomposition methods here reported.

Based on these conclusions, it recommended that the *Divide and Conquer framework* be adopted in future research on the applications of parallel computation to the solution of partial differential equations. Then, *the performance goal* is defined in terms of the *execution time goal*, as

$$T_{DC}(p,n) \equiv T(1, n/p) \qquad (13.1)$$

Or, the *speedup goal*,

$$S_{DC}(p,n) \equiv \frac{T(1,n)}{T(1,n/p)} \qquad (13.2)$$

Or, the *divide and conquer efficiency*:

$$E_{DC}(p,n) = \frac{T(1,n/p)}{T(p,n)} = \frac{S(p,n)}{S_{DC}(p,n)} \qquad (13.3)$$

Acknowledgment

REFERENCES

Herrera I. & Contreras I. "Evidences that Software Based on Non-Overlapping Discretization is Most Efficient for Applying Highly Parallelized Supercomputers to Solving Partial Differential Equations" Chapter 1 of the book "High Performance Computing and Applications", J. Xie et al. (Eds.), Lecture Notes in Computer Science (LNCS), Springer-Verlag, pp. 1-16, 2016. DOI: 10.1007/978-3-319-32557-6_1

Herrera, I., de la Cruz L.M. and Rosas-Medina A. "Non-Overlapping Discretization Methods for Partial, Differential Equations". Numer Meth Part D E, 30: 1427-1454, 2014 (Open source).

Herrera, I. & Rosas-Medina A. "The Derived-Vector Space Framework and Four General Purposes Massively Parallel DDM Algorithms", EABE (Engineering Analysis with Boundary Elements), 37 pp-646-657, 2013.

Herrera I., Contreras I. "An Innovative Tool for Effectively Applying Highly Parallelized Hardware to Problems of Elasticity". Geofísica Internacional, 55 (1) pp., 39-53, 2015.

Herrera, I. "Theory of Differential Equations in Discontinuous Piecewise-Defined-Functions", Numer Meth Part D E, 23(3), pp 597-639, 2007.

Herrera I. and R. Yates "Unified Multipliers-Free Theory of Dual Primal Domain Decomposition Methods". Numer. Meth. Part D. E. 25:552-581, 2009.

Herrera, I. & Yates R. A. "The Multipliers-free Domain Decomposition Methods" NUMER. METH. PART D. E. 26 pp874-905, July 2010. (DOI 10.1002/num. 20462)

Herrera, I. & Yates R. A. "The Multipliers-Free Dual Primal Domain Decomposition Methods for Nonsymmetric Matrices" Numer. Meth. Part D. E. 27(5) pp. 1262-1289, 2011.

DDM Organization, Proceedings of 25 International Conferences on Domain Decomposition Methods www.ddm.org, 1988-2018.

Toselli A. and O. Widlund, "Domain decomposition methods- Algorithms and Theory", Springer Series in Computational Mathematics, Springer-Verlag, Berlin, 2005, 450p.

Dohrmann C.R., A preconditioner for substructuring based on constrained energy minimization. SIAM J. Sci. Comput. 25(1):246-258, 2003.

Mandel J. and C. R. Dohrmann, Convergence of a balancing domain decomposition by constraints and energy minimization, Numer. Linear Algebra Appl., 10(7):639-659, 2003.

Mandel J., Dohrmann C.R. and Tezaur R., An algebraic theory for primal and dual substructuring methods by constraints, Appl. Numer. Math., 54: 167-193, 2005.

Farhat Ch., and Roux F. A method of finite element tearing and interconnecting and its parallel solution algorithm. Internat. J. Numer. Methods Engrg. 32:1205-1227, 1991.

Mandel J. and Tezaur R. Convergence of a substructuring method with Lagrange multipliers. Numer. Math 73(4): 473-487, 1996.

Farhat C., Lessoinne M. LeTallec P., Pierson K. and Rixen D. FETI-DP a dual-primal unified FETI method, Part I: A faster alternative to the two-level FETI method. Int. J. Numer. Methods Engrg. 50, pp 1523-1544, 2001.

Farhat C., Lessoinne M. and Pierson K. A scalable dual-primal domain decomposition method, Numer. Linear Algebra Appl. 7, pp 687-714, 2000.

Klawonn A., Lanser M. & Rheinbach O. "Toward extremely scalable nonlinear domain decomposition methods for elliptic partial differential equations", SIAM J. SCI. COMPUT., Vol. 37, No.6, pp. C667-C696, 2015.

Smith B., P. Björstad & W. Gropp, "Domain Decomposition: Parallel Multilevel Methods for Elliptic Partial Differential Equations", Cambridge University Press, 621p, 1996

Toivanen J., Avery P. and C. Farhat "A multilevel FETI-DP method and its performance for problems with billions of degrees of freedom", Int. J. Numer Methods Eng. 2018; 116:661-682.

L. R. Scott, T. W. Clark, and B. Bagheri"Scientific Parlallel Computing", Princeton University Press, 2005.

Mathew, T. "Domain Decomposition Methods for the Numerical Solution of Partial Differential Equations", Lecture Notes in Computational Science and Engineering. Springer Publishing Company, Incorporated. 2008.

Herrera, I., D.E. Keyes, O.B. Widlund and R. Yates "Domain decomposition methods in science and engineering", Proceedings of the Fourteenth International Conference on Domain Decomposition Methods, Cocoyoc, Mexico, 490pp., 2002.

Ristov S., Prodan R., Gusev M., Skala K. Superlinear "Superlinear Speedup in HPC Systems: why and when?" Proc. of the Federal Conference on Computer Science and Information Systems, pp. 889-898, 2016.

Distribution and current status of permafrost in the highest volcano in North America: Citlaltepetl (Pico de Orizaba), Mexico

Víctor Hugo Soto Molina and Hugo Delgado Granados

Resumen

Se enfatiza la presencia de permafrost en el volcán Citlaltépetl y se actualiza su cubertura. Mediante el análisis empírico-estadístico de variables topo-climáticas y con base en el modelo de regresión lineal fue posible determinar que el límite inferior de permafrost continuo se ubica por encima de 4,880 msnm en la ladera norte y por arriba de 4,963 msnm en su ladera sur; por su parte, porciones discontinuas y aisladas inician a partir de 4,780 y 4,863 msnm al norte y sur del cono volcánico respectivamente. Se encontró una alta correlación entre la temperatura de los perfiles del suelo y la del aire en su altitud correspondiente. Las condiciones de temperatura del permafrost permiten considerarlo como "cálido", tal como sucede en montañas de mediana y baja latitud, y al mismo tiempo se puede clasificar como "comprometido" y potencialmente inestable. No obstante la degradación que presenta a partir de su primera estimación en los años 1970, se estima que este indicador de cambio climático de alta montaña permanezca al menos durante algunas décadas una vez que el glaciar del Citlaltépetl se haya extinguido.

Palabras clave: Permafrost, Citlaltépetl, Cambio climático, Temperatura del aire, Temperatura del suelo, Regresión lineal.

Abstract

The occurrence of permafrost in the Citlaltepetl volcano was emphasized and its coverage was updated. Through an empirical and statistical analysis of topo-climatic variables and based on linear regression it was found that the lower limit of continuous permafrost is positioned above 4,880 masl on its northern slope and at 4,963 on the southern slope; on the other hand, discontinuous and isolated patches start at 4,780 and 4,863 meters in the north and south respectively. A high correlation was found between the temperature of the ground profiles and the air temperature at their corresponding altitude. The temperature found in the permafrost classifies it as "warm" permafrost as in most mountains of medium and low latitude and at the same time it is classified as "compromised" and potentially unstable. In spite of the degradation observed from its first estimation during the 1970s, it is estimated that this indicator of climatic change in high mountains will remain at least for a few decades after the Citlaltepetl´s glacier has been extinguished.

Keywords: Permafrost, Citlaltepetl, Climate Change, Air temperature, Ground temperature, Linear regression.

V. H. Soto Molina
H. Delgado Granados
Departamento de Vulcanología
Instituto de Geofísica
Universidad Nacional Autónoma de México
Ciudad Universitaria
Delegación Coyoacán, 04510
Ciudad de México, México
Corresponding author: islaveracruz@gmail.com

Introduction

Among the four components of the planet's cryosphere (Williams, 2012): floating ice, seasonal snow, glaciers and permafrost, the last three are present in the upper part of the highest Mexican volcanoes: Citlaltepetl, Popocatepetl and Iztaccihuatl [5,610, 5,500 and 5,220 masl respectively (INEGI, 2017)]. Throughout the world, the high mountain landscape is evolving in an accelerated manner as a consequence of climate change (Spehn et al., 2005, Ahumada *et al*., 2010). Of their permanent ice, glaciers have dramatically retreated (Delgado-Granados, 2007; Herrera and Ruiz, 2009) or have been extinct for the past decades, and permafrost (Williams and Smith, 2008) has been degraded in recent years; at the same time, the permanence of seasonal snow has been progressively reduced. This together has forced the periglacial environment to experience geomorphological changes of different magnitude (Ahumada *et al.,* 2010); from the increase in areas of gelifluction (Janke *et al*., 2011), to rock fall and landslide with catastrophic results (Etzelmüller, 2013). Several investigations (Gruber *et al.,* 2004, Huggel *et al*., 2010, Clague *et al*., 2012) document that in many cases the degradation of permafrost has been the main conditioning factor.

Permafrost is a strictly thermal condition of the ground (French, 2007), and it is present in circumpolar regions as well as in some high mountain areas of medium and low latitude such as the Alps and the Andes especially; there are isolated mountains in regions of the tropics that also contain it. It is composed of rock or soil with or without the presence of organic elements in its interior that remain at least two continuous years below 0 ° C (Trombotto *et al.,* 2014); Above this is the active layer that is characterized by a cyclical freezing and thawing in response to the seasons of the year (Osterkamp and Jorgenson, 2009). Due to the physical-chemical characteristics of the soil and external processes such as the infiltration of water by melting and precipitation, the ice inside it may be present although it is not strictly necessary (French, 2007). To indicate the general characteristics of its coverage it is designated as "continuous permafrost" when it is present in more than 90% of the surface of the land; "discontinuous permafrost" is between 65 and 90% and "sporadic" below 65% (Trombotto *et al*., 2014).

Unlike the near-polar regions, the heterogeneity of the high mountain relief establishes the existence of microclimates among relatively small areas (Haeberli *et al.,* 2010) that often condition that air temperature and the correspondence with the presence of permafrost may differ substantially from the air-ground correlation present in circumpolar areas (Guodong and Dramis, 1992). While in Canada and Alaska the lower limit of continuous permafrost generally corresponds to an annual average air temperature (AAAT) of -6°C (Smith and Riseborough, 2002) and the discontinuous permafrost limit coincides with the annual isotherm of -1°C (Brown, 1970; French and Slaymaker, 1993), in mountains of medium and low latitude many times the presence of permafrost can occur with a AAAT above 0°C (Guodon and Dramis, 1992); such is the case of the Sierra de Telera, Spain (Andrés y Cía, 2006) and the Mauna Kea volcano, Hawaii with a AAAT of + 3.6°C (Woodcock, 1974, Gorbunov, 1978).

The periglacial environment in Mexico and particularly the topic of permafrost was addressed in glaciological studies at the end of the 1960s (Lorenzo, 1969a, Lorenzo, 1969b) and even more so during the 1970s through the studies of Heine (1973, 1975a, 1975b). , 1977), as well as Gorbonov (1978). Specifically, Heine (1975) performs a periglacial inventory on the Citlaltepetl volcano based on strictly visual descriptions, noting, in addition to other geomorphological features, that the lower limit of permafrost is located at 4,600 meters above sea level (masl). Again in the 1990s Heine (1994) reiterates the discontinuous presence of permafrost in the high Mexican mountains above the 4,600 level. During the last twenty years, most systematic works for the determination of permafrost in the country have begun, considering the thermal variable of the ground. These more recent researches have been carried out in the Popocatepetl and Iztaccihuatl volcanoes exclusively (Palacios et al., 2007, Andrés *et al.,* 2010, 2011, 2012), leaving aside the Citlaltepetl volcano, the highest in the country and in North America.

In the light of the above, this work has a dual purpose: in the first instance it aims to complement the most recent studies on permafrost in the three highest mountains in Mexico and secondly, it seeks to indicate the current state of its coverage in Citlaltepetl, which, in view of the current climate change conditions should be different from the one pointed out 43 years ago. The investigation is approached by analyzing the temperatures of ground profiles at different depths and their correlation with the AAAT; the degree of incidence of solar radiation on the surface and the albedo indexes are analyzed so that together the presence and limits of permafrost are indicated. The permanent existence of ice in the subsoil and rock confirms the above.

Geographic generalities of the study area

The volcano Citlaltepetl (Star hill in Nahuatl) or Pico de Orizaba is a stratovolcano that belongs to the Neo Volcanic Axis of Mexico in its easternmost area. The center of its crater is located at coordinates 97 ° 16' N and 19 ° 02' E (Rossotti *et al*., 2006). It has an altitude of 5,610 masl (INEGI, 2017) which makes it the highest volcano in North America and the third largest mountain after Mount Denali (6,190 masl) and Mount Logan (5,959 masl). Its age is dated in ~ 650,000 years when the first stage of formation known as "Torrecillas" began, which was followed by two more phases of evolution including "El Espolón de Oro" and the current crater (Macias, 2005). The most recent geological formations are a consequence of this last eruptive phase between 16,500 and 4,000 years ago (Macías, 2007); these are generally composed of dacite and andesite flows that cover large extensions of the north of the cone, some parts have been buried by deposits of pyroclastic material and ash; many of these materials have been compacted and others have a looser consistency (Carrasco-Núñez and Rose, 1995). The southern slope presents a significant flow of andesite from the same period and is mostly covered by pumice deposits that cover a large part of this slope with a gray-white color. The eastern and western slopes have lower amounts of lava flows that combine with deposits of pumice and ash. Above 4,000 masl the gelifraction process of the rock is noticeable, which in some cases forms conical deposits that flow according to the slope. The volcano has a clearly conical structure; the lava flows are located below the 4,900 level and above this limit its shape is markedly regular and homogeneous. On its north face and above 5,060 masl the glacier begins, extending continuously to the crater at the top of the cone; this summit divides the states of Puebla and Veracruz. In the slopes of the state of Puebla, the orography is very regular until it connects with the Central Mexican High Plateau with an average altitude of 2,200 masl; on the other hand, the relief is more rugged on the Veracruz side until it connects with the coastal plains of the Gulf of Mexico.
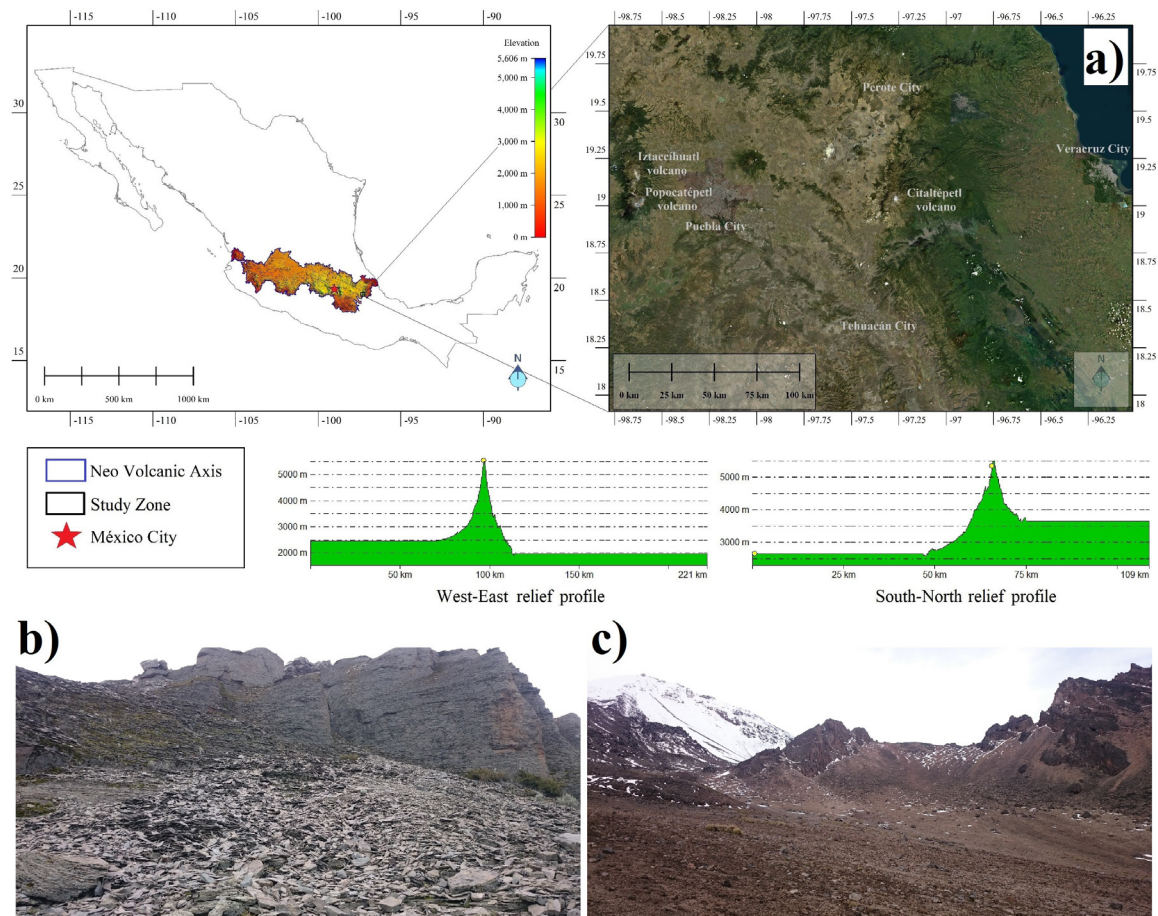

Figure 1. Study zone. Prepared by authors.

Materials and methods

To understand and indicate the presence of permafrost requires the combination of models and physical observations due to the systematic variability caused by the orography of the environment, which tends to be different from one area adjacent to another (Gruber and Haeberli, 2009). For this reason, in this work the current coverage of permafrost in the volcanic cone is evidenced and indicated through of a Geographic Information System (GIS) and under an empirical-statistical approach of topo-climatic variables [Julián and Chueca (2004), Julián and Chueca (2005), Abramov et al., (2008) and Serrano *et al*. (2009)].

Temperature

To confirm the presence of permafrost and to delimit its coverage under the thermal criteria, five observation stations were installed for the temperature of the sub-soil and air. Four of these stations were placed at different altitudes on the northern slope of the volcano and one more on the southern slope. To the north, the first one was installed at the timberline at 4,050 masl; the second at 4,200 masl, the third at 4,584 masl and the last near the lower limit of the glacier (5,060 masl). The southern station was placed under conditions similar to that of the northern elevation of 4,200, both in altitude and in the type of substrate and orographic conditions. At each station the ground was drilled to where the substrate and tools allowed under the PACE technical manual standards (Harris *et al.,* 2001) and the IPA (2008). In each perforation, a 2 "diameter PVC pipe was introduced, which was sealed at both ends; inside, Hobo Pendant UA-001-64 sensors were programmed and placed to log data every hour from March 22, 2015 until December 10, 2017. However, in order to avoid any uncertainty caused by considering incomplete years or seasons, the data analysis period for this work was two full years between July 1, 2015 and June 30, 2017. A sensor with the same characteristics was placed near each borehole to record the air temperature in equal periods. Figure 2 shows the position of the stations and the depths of each sensor.

Station	Longitude	Latitude	Altitude (masl)	Depth of sensors (cm)
1	-97°16′29.5′′	19°04′20.8′′	4,050	-5, -30, -60, -120
2	-97°16′23.9′′	19°03′36.8′′	4,200	-5, -40, -100, -175
3	-97°16′12.5′′	19°02′46.7′′	4,584	-5, -30, -60, -80
4	-97°16′10.6′′	19°02′23.6′′	5,060	-5, -50
5	-97°16′29.5′′	19°00′18.2′′	4,200	-5, -40, -100
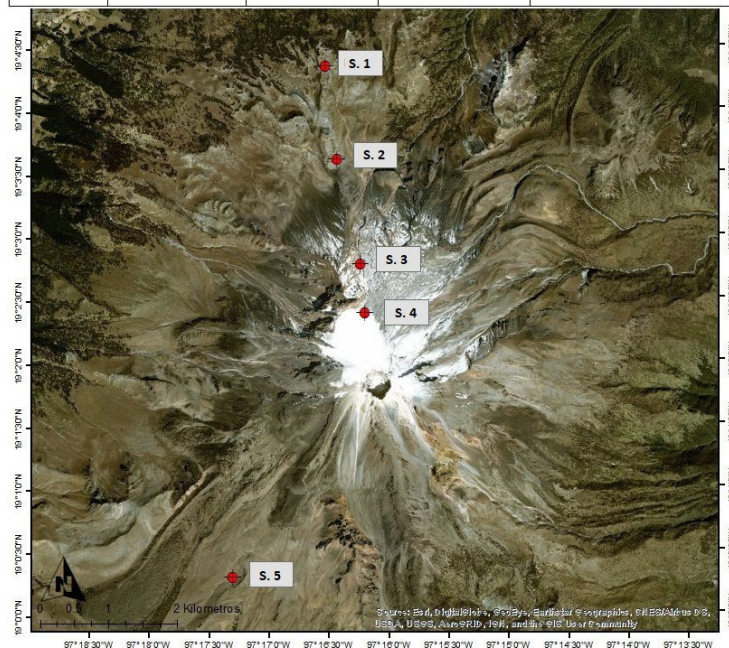
Figure 2. Location of the stations and depth of the sensors. Drilling at 5,060 masl was limited to only 50 cm due to the hardness of the frozen ground that was found. Prepared by authors.

The extraction and backup of the data was done every three months on average and during each visit the status of the batteries was tested; when they marked less than 50% of life they were replaced by new ones. The main objective of these tasks was to keep the sensors in optimal conditions for an uninterrupted temperature record and free of any alteration outside the characteristics of the weather that together would result in complete and homogeneous data series (Aguilar *et al*., 2003, OMM, 2011, Firat *et al.,* 2012).

The data of the two years were divided by month for each of the series and the monthly average was obtained, as well as the value of the annual average of both the air (AAAT) and the ground (AAGT) in the different depths to observe its oscillations throughout the year. In addition, monthly ground data were plotted along with their annual average value to analyze the temperature trend according to depth based on Williams and Smith (1989). At the same time the summer and winter periods were traced to further strengthen in the calculation of its temperature. Once the trend lines for the colder and warmer periods were joined at a point that manifested the absence of thermal oscillation between the two will mark the AAGT of each profile, and if this was within the range of negative temperatures would indicate the presence of permafrost (van Everdingen, 1985; French, 2007; Heginbottom *et al*., 2012). To determine the altitudinal limit of the permafrost, the equation of the regression line resulting from the correlation between the temperatures of the ground profiles and the altitude at which they are located was used; to ensure the quality of the estimation, statistical tests were performed on the residuals of the linear regression. Additionally, the AAAT records were used to compare with the AAGT of each profile; if the AAAT was negative at an altitude with a thermal profile that indicated the presence of permafrost, there would be an ideal air-ground correlation as suggested by Brown (1970), French and Slaymaker (1993) and Smith and Riseborough (2002). On the other hand, if the AAAT were higher than 0 ° C with a ground profile with permafrost, it would emphasize what was pointed out by Woodcock (1974), Gorbunov (1978), Guodong and Dramis (1992) and Andrés y Cía (2003).

Orography and incident solar radiation

In order to consider the different features of the relief, a digital terrain model (DTM) with a resolution of 2 meters per pixel was used. From this, the altitude as well as the aspect and slope characteristics were analyzed to determine the incident solar radiation (ISR). The ISR was calculated in ranges from low to high considering the values of the summer and winter solstices for a year through the Solar Radiation tool of ArcGis 10.4 which in turn is based on the algorithms of Fu and Rich (2000, 2002).

Albedo

It is widely documented that surface albedo greatly governs surface temperature when it comes to ISR (Liang *et al*., 2010). To observe the albedo index in the volcanic cone in ranges from 0 to 1 [considering that 0 represents a total absorption of incident solar energy and 1 is equivalent to the total reflection of that energy (Arya, 2001; Dobos, 2003)], a Landsat-5 satellite image with a resolution of 30 meters was used. Special care was taken to choose a cloud-free image over the study area and in a season totally free of seasonal snow. For this purpose, the image LT05_L1TP_025047_2009 1212_20161017_01_T1 was obtained from the USGS through the Earth Explorer platform. The surface albedo was obtained by the proposal of Liang (2000) and Liang *et al.* (2002) through the combination of bands 1, 3, 4, 5 and 7 by the equation:

$$\alpha = \frac{0.356_{p1} + 0.130_{p3} + 0.373_{p4} + 0.085_{p5} + 0.072_{p7} - 0.0018}{0.356 + 0.130 + 0.373 + 0.085 + 0.072}$$

(1)

Where "α" is the albedo per pixel in the image, "p" is the band number and the values in thousandths correspond to the conversion factor for each of them. The processing was developed with the Map Algebra tool of ArcGis 10.4.

Once the presence of permafrost was determined directly by the temperature of the ground profiles and its altitude was delimited by linear regression, both the ISR and the albedo served to identify areas that despite being located tens of meters vertically below the limit lower of continuous permafrost, its low ISR range and a high albedo index, both in comparison to the values present in the zones previously identified through its temperature, allowed to consider them as areas of discontinuous permafrost that included isolated or sporadic patches. The visual recognition of ice in the subsoil (French, 2007) as interstitial or covered ice (Trombotto *et al.,* 2014) that remain throughout the year (Williams and Smith, 2008) and its georeferencing allowed to corroborate these areas. Finally the surface for each type was calculated with the Surface volume tool of ArcGis 10.4 considering the DTM to obtain the value of each area according to the altitude of the relief.

Results

The behavior of the monthly air temperature in each station shows an oscillatory pattern throughout the year that can be considered highly correlated (Motulsky and Christopoulos, 2003) in relation to the altitude at which they are located [Figure 3 (f)]. At 4,050 masl the range goes from 3.45 to 7.58°C and an AAAT of 4.97°C; at 4,200 masl, the thermal range is the lowest of all with values between 3.68 and 6.86°C and an annual average of 4.87°C. In level 4,584, the widest annual oscillation is recorded with values between -2.94 and 2.49°C with an average of 0.29°C. At 5,060 masl it varies from -2.99 to 1.06°C with an AAAT of -0.46°C. The southern station at 4,200 masl has a very similar oscillatory range, although slightly colder than its equivalent on the northern slope; their values range from 2.66 to 5.91°C with an annual average of 4.31°C. These patterns of behavior can be seen in Figure 3.

In the same way, the temperature profiles per altitudinal floor are shown in figure 4.

In ascending order of altitude, in the northern slope the temperatures found in the ground profiles are: at 4,050 masl, 7.80°C; at 4,200, 7.00°C; at 4,584 masl, 1.10°C and finally permafrost was located at elevation 5,060 with a temperature of -0.35°C. By using the regression equation of figure 4 (f) to determine the height at which the ground temperature is maintained at <= 0 ° C throughout the year, it is found that the lower limit of continuous permafrost is located at 4,880 masl. Figure 5 shows in summary the altitudinal estimate (shaded in black) and its statistical analysis.

A higher AAGT in the profile of the southern station is due to a greater amount of ISR [see figure 7 (a)]; it shows a value of 7.80°C at 4,200 masl. Considering the 0.80°C difference between the north and south profiles at 4,200 masl, it is assumed that the lower limit of the
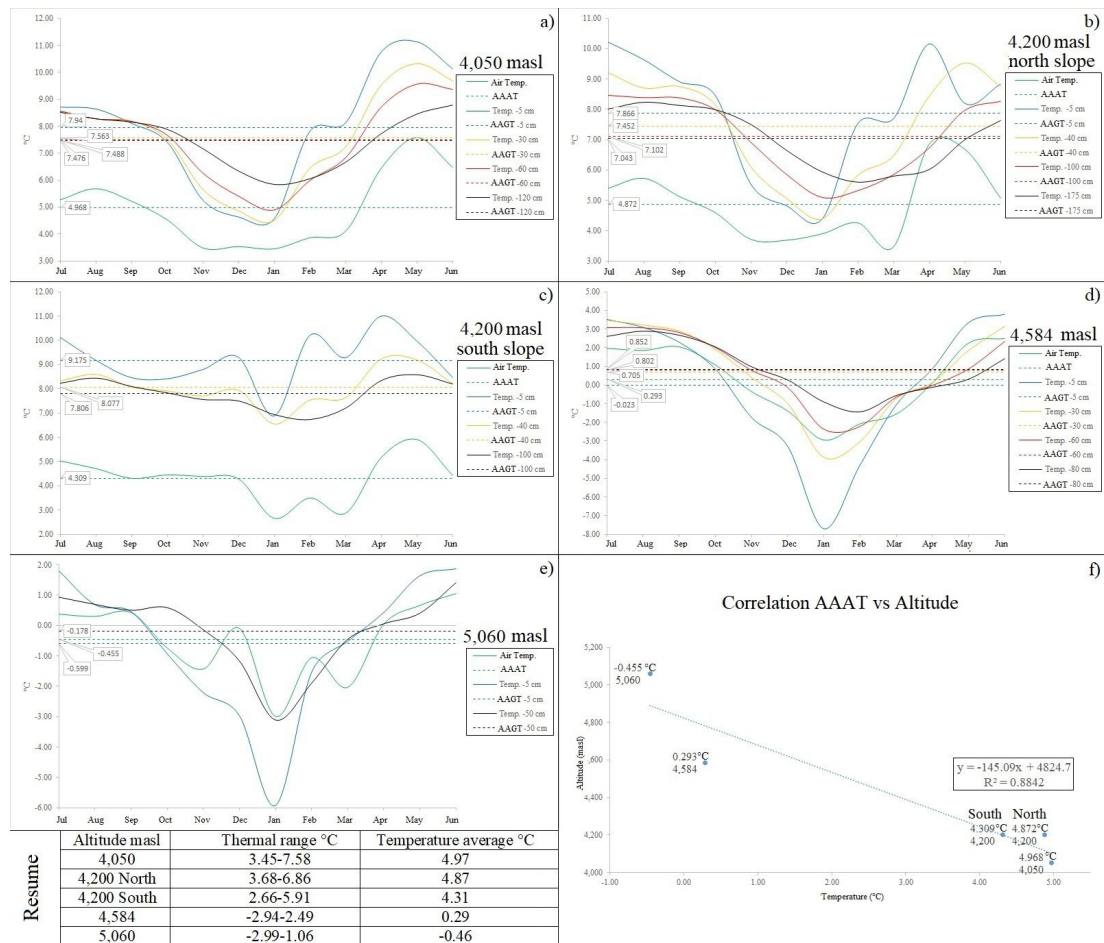

Figure 3. Monthly air and ground temperatures 2015-2017. The graph "f" indicates the correlation between the AAAT and the altitude of each station.
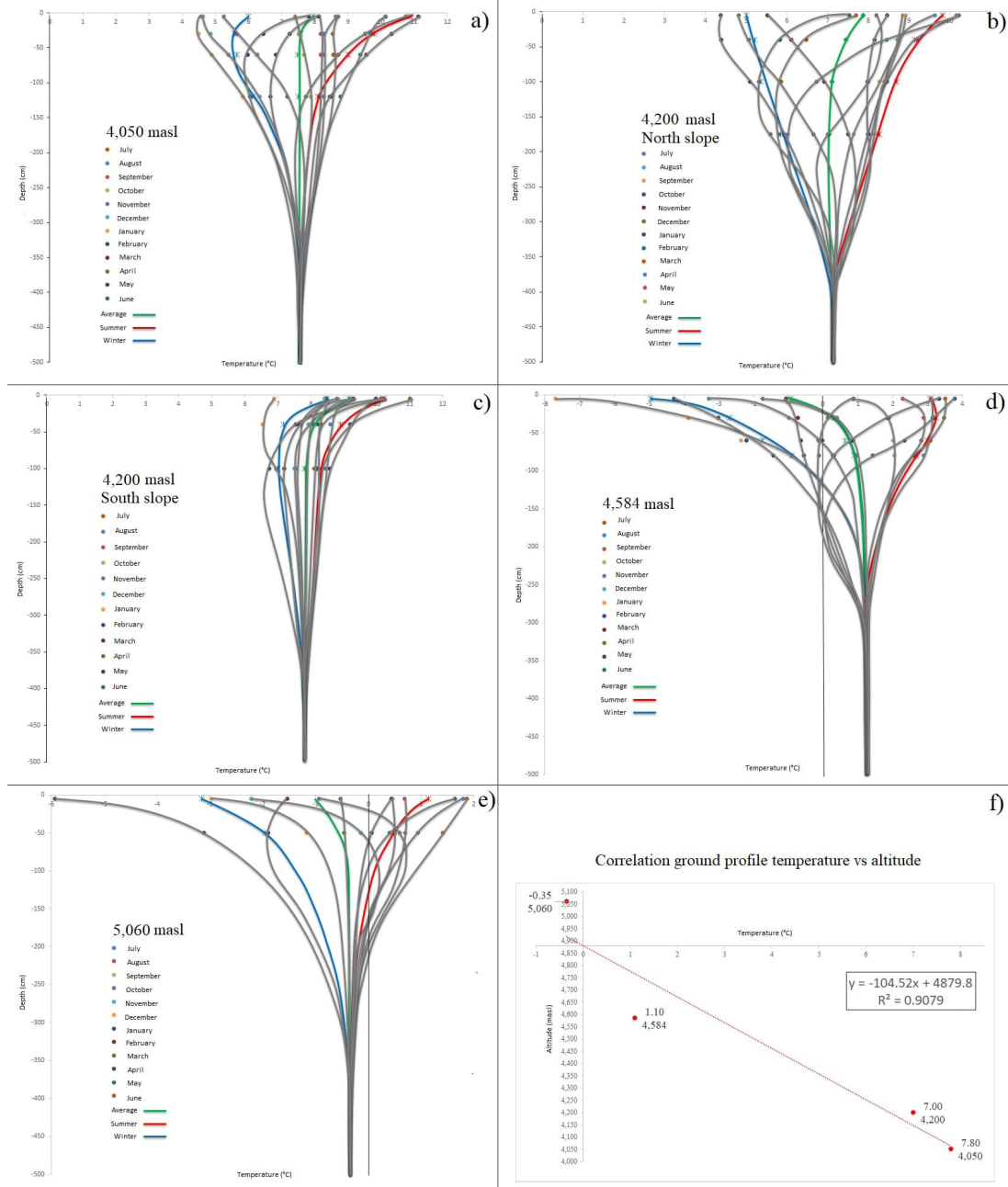
Figure 4. Monthly temperatures of the ground profiles 2015-2017. The graph "f" indicates the correlation with the altitude on the north slope. The crossing of axes "X" and "Y" is justified below.

continuous permafrost is located above the corresponding limit on the north side. In this way, if we use the previous regression equation once more to identify at what altitude the line crosses the -0.80°C we obtain as a result 4,963 masl as seen in figure 5. That is, while in the north the lower limit of continuous permafrost with a TMAS <= 0°C is located at 4,880 masl, in order to match that temperature in the south it would be necessary to ascend 83 meters

more in vertical; so the permafrost cover, given the conical geometry of the volcano, would represent a concentric and at the same time elliptical shape (see figure 11). On the other hand, concerning the temperature of each profile and the value of the air temperature at the altitude at which they are located, there is an almost perfect correlation (Motulsky and Christopoulos, 2003) with R^2 = 0.99; this relationship is summarized in Figure 6.
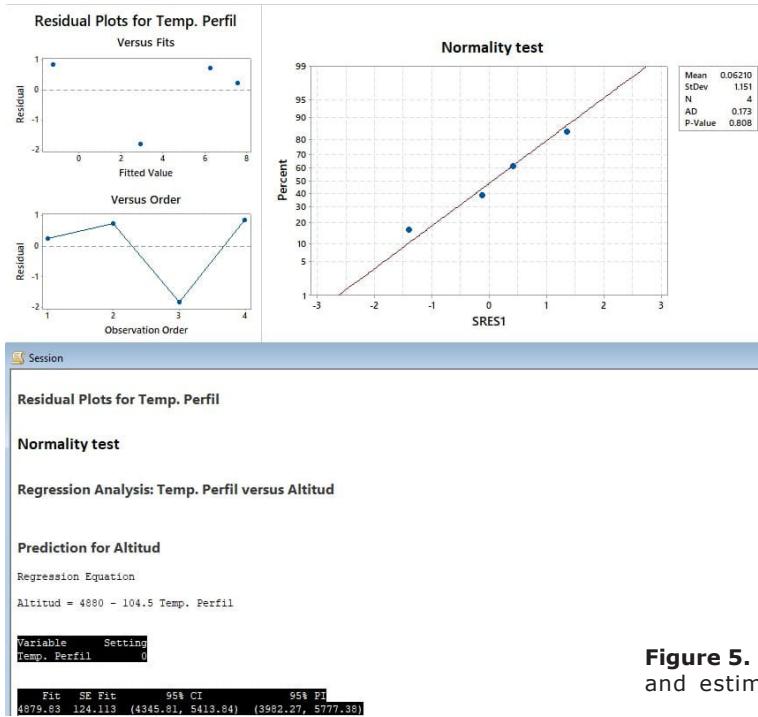
Figure 5. Regression analysis by means of residuals and estimation of the lower altitudinal limit of permafrost.
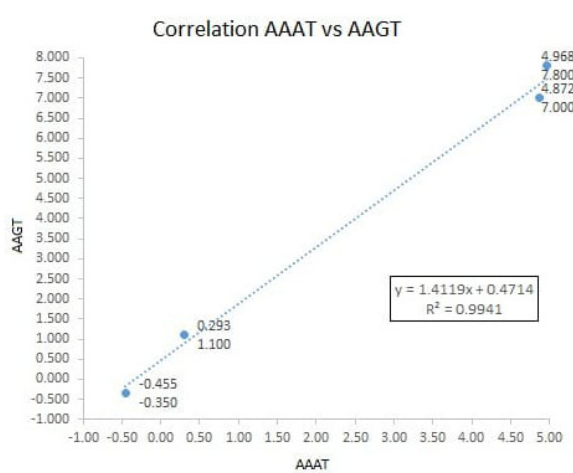
Figure 6. Air-ground correlation on the northern slope of the volcano. In this analysis, the southern slope station was not considered because, despite having an AAGT greater than that of its northern equivalent in response to a greater ISR, it has (as noted above) an AAAT 0.56°C lower.

Regarding the characteristics of the relief and its determining role on the ISR throughout the year, it can be seen in the map of figure 7 (a). In the same way, the particularities of reflection of the deposits determine the albedo indexes shown in the resulting map of Figure 7 (b).

The prospecting carried out along with the data mining allowed to identify large portions of ice buried by debris flows and deposits of

finer materials above 4,700 masl. The location of these portions of buried ice suggest that they are remnants of the glacier which extended to this level during the year of 1975 (Cortés-Ramos and Delgado-Granados, 2015).

Additionally, ice outcrops are common through the rocky walls; many of these have remained throughout the time this work lasted, particularly those that are above 4,700 masl. The series of images shown in figure 9 provides an example of this.

There is also another type of geoform composed of detritus and cryoclasts with ice developed inside just below the set of nivodentritic channels at the foot of the remains of "El Espolón de Oro". The rich ice content in its interior could be the product of snow accumulation that has been covered by debris over time; it is suggested, according to Trombotto et al., (2014) that it could represent a phase in the evolution of a debris glacier.

Therefore, it can be assumed that at least one hundred meters below the limit of continuous permafrost a parallel strip with a discontinuous and isolated presence of permafrost is located, which overall looks in accordance with figure 11.

Finally, the value of the areas of continuous and discontinuous permafrost cover, considering the orography, were estimated at 5.52 km² [this value does not consider the area of 0.61 km²
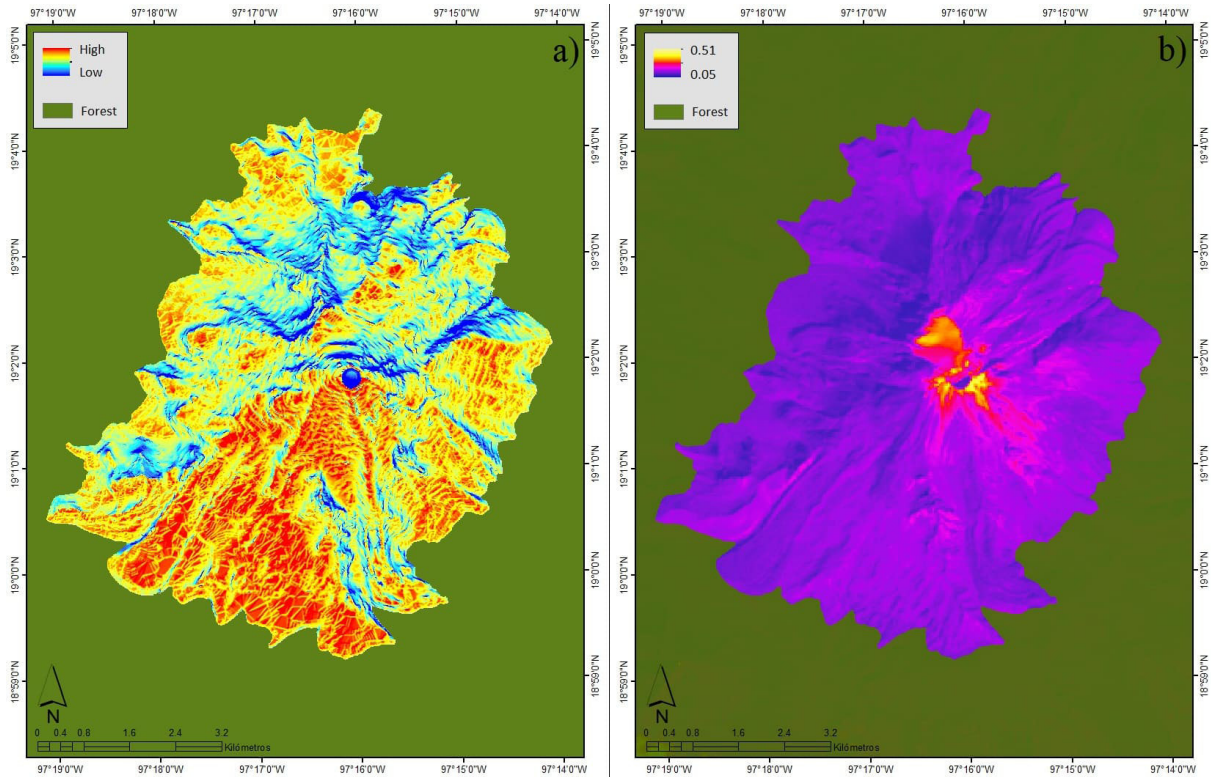
Figure 7. ISR (a) and albedo (b) maps. The highest albedo portion to the north of the crater belongs to the body of the glacier, while the rest are due to the reflectivity of the pumice deposits (Dobos, 2003, Ahrens, 2006). Prepared by authors.
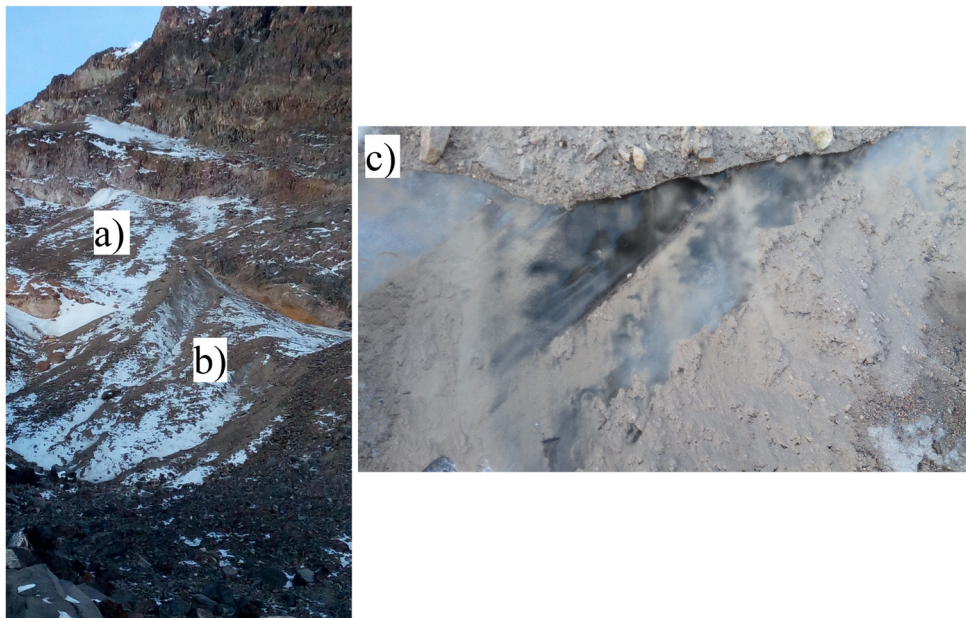
Figure 8. Buried ice in the northern slope. The image was taken at 4,810 masl, just below the "El Espolón de Oro"; it shows two isolated patches (a and b) of glacial ice buried by debris with a diameter of 2 to 12 cm. The linear section of exposed ice of patch b has a thickness of 60 cm and a length in the direction of the slope of approximately 65 meters. Photograph (c) shows in detail an exposed portion of solid ice below fine sediments and gravel.
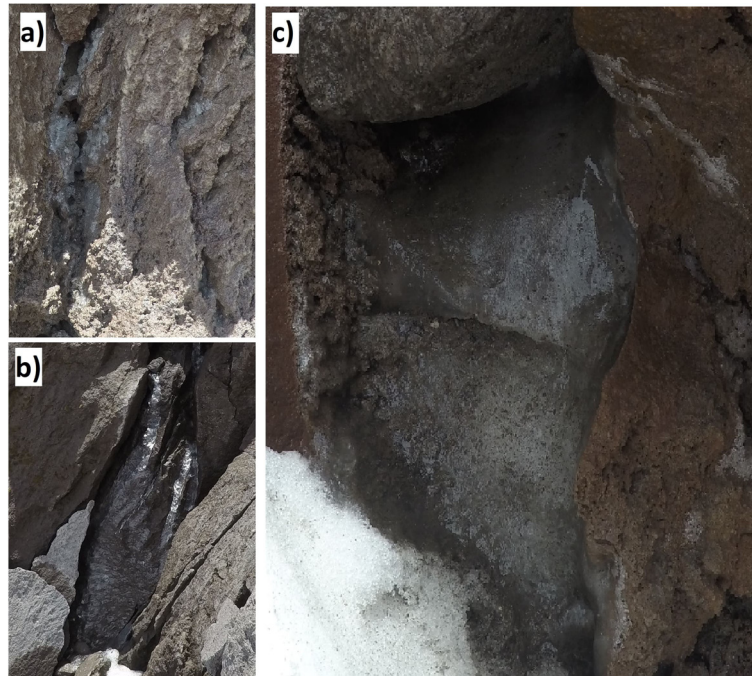
Figure 9. Interstitial and intrusive ice. The sequence of previous photographs was taken at mid-day on May 31, 2016. The photo (a) was taken at 4,780 masl in the rocky portion known as "Los laberintos" and is visible through the cavities of the rock the lenticular ice agglomerations of 1 to 2 cm in diameter. Photo (b) shows a larger portion of ice that has formed in the middle of the separation of blocks of dacite from the flow of "Los laberintos" at 4,730 masl; it can be noticed the diagonally shaped 60 x 20 cm expanded between the spaces of the rock. The photograph (c) was taken close to 4,800 masl; the external part of approximately 90 x 40 cm of a solid portion of ice that covers the entrance of a rock cavity is clearly visible.
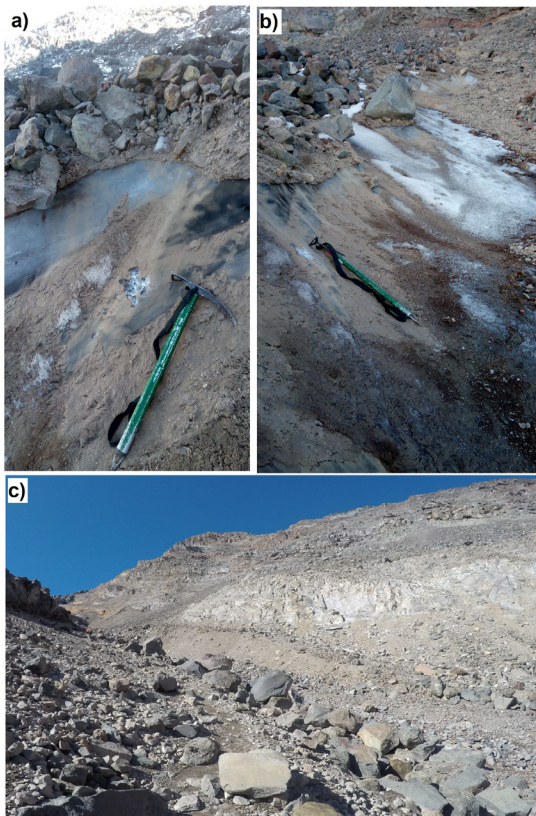
Figure 10. Protalus rampart on the northern slope. The photograph (a) shows the rich ice content by the recrystallization of the snow; in the background a part of the group of snow-debris channels can be seen. The exposed portion of massive ice shows a lobular shape that extends from the middle of the geoform to the upper part of it (photograph b). The photograph (c) was taken from an altitude of 4,700 masl; it exhibits the whole of the geoform that starts at 4.765 masl with an almost angular aspect close to the middle of its shape, product of the debris bearing above it that turn in the direction of the small valley downhill. In the background the summit of the "El Espolón de Oro" can be observed.
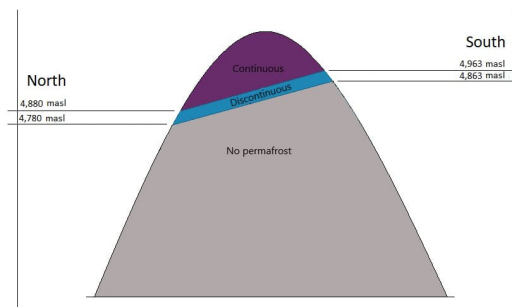
Figure 11. Schematic distribution of permafrost in the volcanic cone. The image has been made without considering scales. Prepared by authors.

(Cortés-Ramos, 2016) occupied by the glacier] and 2.06 km^2 respectively.

After the combination of variables, factors and elements analyzed in this paper, we can obtain the final map of permafrost distribution in the Citlaltepetl volcano (figure 12).

Discussion

After 43 years, when Heine (1975) pointed out the presence of permafrost in the volcano, it is still present in the Citlaltepetl. Although the author did not have prolonged temperature records to determine the permanence of the ground under freezing over at least two continuous years as is currently indicated in the specialized literature, this work confirmed its presence from the thermal perspective. The isolated and discontinuous portions that Heine found from 4,600 masl today are 180 meters above, an area we have identified as the discontinuous permafrost strip with an area of 2.06 km^2. On the other hand, the continuous permafrost cover is positioned at an average of 4,920 masl, considering the north and south slopes with an area of 5.52 km^2. The homogeneous characteristics of the relief and the material deposited above this level condition the continuous presence of permafrost.

The degradation of permafrost in the Citlaltepetl, although it is remarkable, has been presented more slowly compared to the retreat of its glacier. If we consider the northern slope where Heine (1975) indicates its beginning at 4,600 masl and that for that same year the lower limit of the glacier was calculated at 4,700 masl (Cortés-Ramos and Delgado-Granados, 2015), to compare it against our estimate of the discontinuous permafrost from 4,780 masl and currently at the beginning of the glacier at 5,060 masl, we obtain a retraction of 360 meters in the glacier against 180 meters of variation in the permafrost limit; in other words, the glacier has retreated at a rate of 8.6 meters per year compared to 4.3 meters per year of permafrost since 1975. These circumstances indicate the persistence of permafrost before the possible extinction of the glacier.

The large portions of ice found in the subsoil have remained at least for decades and are likely to remain even after the glacier has disappeared; on the other hand, the smaller fragments embedded in the rock walls may last only a few years due to the high rate of thermal conductivity offered by the rock (Vosteen and Schellschmidt, 2003).
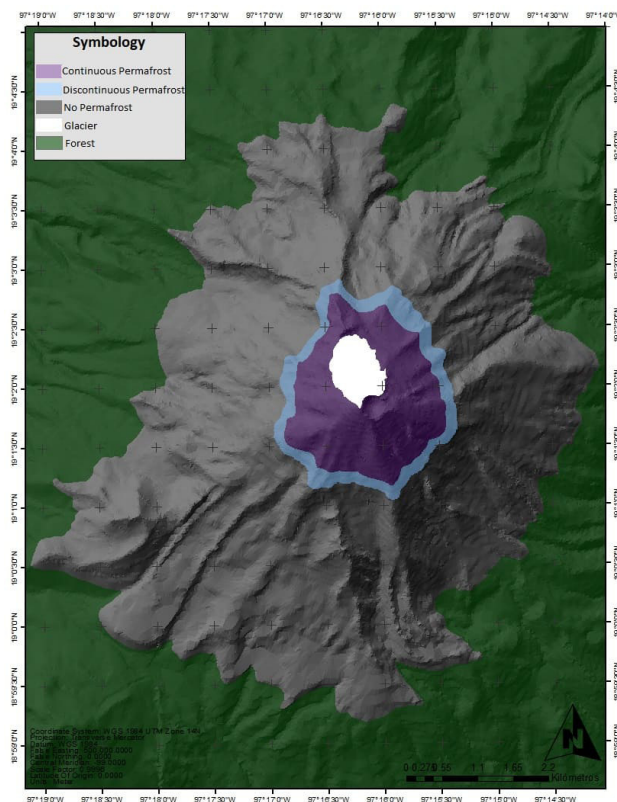
Figure 12. Map of distribution of permafrost in the Citlaltepetl volcano. Prepared by authors.

Although the surface of the south slope receives more ISR throughout the year compared to the north, its higher albedo index would balance its temperature to some extent. In spite of the fact that there is a warmer temperature of 0.56°C in the profile of the southern ground with respect to the north at 4,200 masl, the higher index of albedo above 4,800 masl compared to that of the northern slope at the same elevations and near the top it becomes equal or slightly higher than the one that presents the glacier ice of the north, it would come to "soften" the degree of ISR.

The regression model applied for the estimation of the lower limit of permafrost shows an acceptable level of certainty and is based on the high correlation existing (Motulsky and Christopoulos, 2003) between the AAGT of each profile and its corresponding altitude (R^2 = 0.91).

The AAAT and the AAGT in the north are perfectly matched (R^2 = 0.99). The case of the southern slope, at least for elevation 4,200 where the soil is warmer in response to the aforementioned ISR, the ground-air relationship deserves special attention and should be addressed in subsequent studies because its AAAT could be influenced for other micro-climatic factors.

The presence of permafrost in the station located at 5,060 masl and its corresponding value of air temperature (-0.35°C and -0.45°C respectively), as well as the AAGT-AAAT correlation indicated above indicate that at least for this mountain the permafrost interacts with an air temperature also below zero and at the same time make assume a balance between them.

The temperature conditions found in the permafrost classify it as "warm permafrost" (Noeztli *et al.,* 2003) and coincide very closely with those found by Andrés et al., (2010, 2011) and Yoshikawa (2013) in the tropical Chachani volcano (16 ° south latitude) of the Peruvian Andes and with the most of the high and low latitude permafrost in which its thermal conditions, always close to the thawing point, could allow them to be classified as "committed" and potentially unstable as suggested by Fischer et al., (2006).

Conclusions

The permafrost at Citlaltepetl is still present, but the degradation and retreat of its coverage is latent; this process is relatively similar to that of the retreat of its glacier in response to climate change as expressed by Wiliam and

Smith (2008) and Ahumada et al., (2010). Notwithstanding the above, the rise of the lower limit of permafrost has been slower in comparison, as pointed out on a global scale by Fischer *et al.,* (2006) due to its hiding and protection characteristics provided by the surface and are contrary to direct exposure to the elements experienced by glacial ice. This suggests that of these two indicators of high mountain climate change, permafrost will remain at least a few decades after the glaciers are extinct.

This work updates the information provided in 1975 by Heine and complements the series of more systematic studies on permafrost coverage for the three highest mountains in the country.

Recommendations

Given its importance as an indicator of climate change, a continuous and uninterrupted monitoring of the permafrost temperature in the highest volcano in Mexico and North America, including, among other actions, the expansion of observation stations with records at a greater depth, is highly necessary in order to have a more complete and accurate database that serves as a basis for climate studies and subsequent geological risks.

References

Abramov, A., Gruber, S. and Gilichinsky, D., 2008. Mountain Permafrost on Active Volcanoes: Field Data and Statical Mapping, Klyuchevskaya Volcano Group, Kamchatka, Russia. *Permafrost and Periglacial Process*. Num. 19, pp. 261-277.

Aguilar, E., I. Auer, M. Brunet, et al., 2003. Guidelines on climate metadata and homogenization. WMO-TD No. 1186, WCDMP No. 53. WMO, 55.

Ahumada, A., Ibáñez, G., y Páez S., 2010. Reconocimiento de permafrost andino en las nacientes del río Santa María, Catamarca. *Ciencia*, Vol. 5 (13), pp. 95-110.

Andrés, A. J., & Cía, J. C., 2006. Modelización de la distribución del permafrost en la Sierra de Telera (Pirineo Central Español) a partir del empleo de Sistemas de Información Geográfica. *Rev. C & G.,* 20 (1-2): 25-46.

Andrés N., Zamorano, J., y Vázquez-Selem, L., 2010. Distribución del permafrost e intensidad de los procesos periglaciares en el estratovolcán Iztaccíhuatl (México). *Eria*, Num. 83, pp. 291-310.

Andrés, N., Palacios, D., Úbeda, J. and Alcalá, J., 2010. Ground thermal conditions at Chachani volcano, Southern Peru. *Geografiska Annaler: Series A, Physical Geography*, 93, 151–162. DOI: 10.1111/j.1468-0459.2011.00424.x

Andrés de Pablo, N. D., Estremera, D. P., Palenque, J. Ú., & Reygosa, J. A., 2011. Medio periglaciar, permafrost y riesgos naturales en un volcán tropical extinto: Nevado Chachani (sur de Perú). *Scripta Nova: revista electrónica de geografía y ciencias sociales*, (15), 376.

Andrés, N., Palacios, D., Zamorano, J. J., & Vázquez-Selem, L., 2011. Shallow ground temperatures and periglacial processes on Iztaccíhuatl volcano, Mexico. *Permafrost and Periglacial Processes*, *22*(2), 188-194.

Andrés, N., Palacios, D., Zamorano, J. J., Mendoza_Margain C., y Vázquez-Selem, L., 2012. "Temperatura del suelo en el volcán Popocatépetl: Implicaciones entre actividad volcánica y degladación". VIII Reunión Nacional de Geomorfología, Guadalajara, México.

Arya, P. S., 2001. *Introduction to micrometeorology* (Vol. 79). Academic press 420 pp.

Brown, R. J., 1970. *Permafrost in Canada: its influence on northern development*. University of Toronto Press.

Carrasco-Núñez, G., & Rose, W. I., 1995. Eruption of a major Holocene pyroclastic flow at Citlaltépetl volcano (Pico de Orizaba), México, 8.5–9.0 ka. *Journal of volcanology and geothermal research*, *69*(3), 197-215.

Clague, J. J., huggel, C., Korup, O., McGuire, B., 2012. Climate change and hazardous processes in high mountains. Revista de la Asociación Geológica Argentina, 69 (3): 328-338.

Cortés-Ramos, J., 2016. *Determinación de los regímenes glaciales en los volcanes Citlaltépetl e Iztaccíhuatl: factores físicos del retroceso y evolución glacial en México* (Doctoral thesis). Universidad Nacional Autónoma de México, Ciudad de México.

Cortés-Ramos, J., & Delgado-Granados, H., 2015. Reconstruction of glacier area on Citlaltépetl volcano, 1958 and implications for Mexico's deglaciation rates. *Geofísica internacional*, *54*(2), 111-125.

Delgado Granados, H., 2007. "Climate change vs. Volcanic Activity: Forcing Mexican Glaciers to Extinguish and Related Hazards. Proceedings of the First Internacional Conference on the Impact of Climate Change on High-Mountain Systems", Instituto de Hidrología, Meteorología y Estudios Ambientales, Bogotá, Colombia, pp. 153-168.

Dobos, E., 2003. Albedo, Encyclopedia of Soil Science. DOI: 10.1081/E-ESS 120014334.

Etzelmüller, B., 2013. Recent advances in mountain permafrost research. Permafrost and periglacial Processes, (24): 99-107.

Firat, M., Dikbas, F., Koc, A. C., & Gungor, M., 2012. Analysis of temperature series: estimation of missing data and homogeneity test. *Meteorological Applications*, *19*(4), 397-406.

Fischer, L., Kääb, A., Huggel, C., & Noetzli, J., 2006. Geology, glacier retreat and permafrost degradation as controlling factors of slope instabilities in a high-mountain rock wall: the Monte Rosa east face. *Natural Hazards and Earth System Sciences*, 6(5), 761-772.

French H.M and Slaymaker O., 1993. Canada's cold land mass. In *Canada's Cold Environments*, French HM, Slaymaker O (eds). McGill-Queen's University Press: Montreal; 3–28.

French, H.M., 2007. The periglacial environment (3rd edition). Wiley and Sons, Chichester, 458 pp.

Fu, P., & Rich, P. M., 2000. The solar analyst 1.0 user manual. *Helios Environmental Modeling Institute*, *1616*.

Fu, P., & Rich, P. M., 2002. A geometric solar radiation model with applications in agriculture and forestry. *Computers and electronics in agriculture*, *37*(1-3), 25-35.

Gorbunov, A. P., 1978. Permafrost investigations in high-mountain regions. *Arctic and Alpine Research*, 283-294.

Gruber, S., Hoezle, M., Haeberli, W., 2004. Permafrost thaw and destabilization of Alpine rock walls in the hot summer of 2003. Geophysical research letters, vol. 31, L13504, doi: 10.1029/2004GL020051.

Gruber, S., y Haeberli, W., 2009. "Mountain permafrost" in R. Margesin (ed), *Permafrost Soils*, *Soil biology*, Springer-Verlag, Berlin.

Guodong, C., & Dramis, F., 1992. Distribution of mountain permafrost and climate.*Permafrost and Periglacial Processes*, *3*(2), 83-91.F

Haeberli, W., Noetzli, J., Arenson, L., Delaloye, R., Gärtner-Roer, I., Gruber, S., ... & Phillips, M., 2010. Mountain permafrost: development and challenges of a young research field. *Journal of Glaciology*, *56*(200), 1043-1058.

Harris, C., Haeberli, W., Vonder Mu¨ hll, D. & King, L., 2001. Permafrost monitoring in the high mountains of Europe: The PACE Project in its global context. Permafrost and Periglacial Processes 12, 3–11.

Heginbottom, A., Brown, J., Humlum, O., and Svensson, H., 2012. Permafrost and Periglacial Environments. *In* Williams Jr., Richard S. And Ferrigno, Jane (edts). State of the Earth´s Cryospherre at the Beginning of the 21st Century: Glaciers, Global Snow Cover, Floating Ice, and Permafrost and Periglacial Envoronments. U.S. Geologycal Survey Professional Paper 1386-A. 496 pp.

Heine, K., 1973. Variaciones más importantes del clima durante los últimos 40,000 años en México. *Comunicaciones,* Proyecto Puebla-Tlaxcala (Fundación Alemana de Investigaciones Científicas), 7: 51-58.

Heine, B., 1975a. Permafrost am Pico de Orizaba/Mexiko. *Eiszeitalter u. Gegenwart,* Vol 26, pp. 212-217.

Heine, K., 1975b. *Studien zur jungquartären Glazialmorphologie mexikanischer Vulkane: mit einem Ausblick auf die Klimaentwicklung* (Vol. 7). Steiner.

Heine, K., 1977. Zur morphologischen Bedeutung des Kammeises in der subnivalen Zone randtropischer semihumider Hochgebirge Beobachtungen aus Mexiko in den Jahren 1971-1975. *Z. Geomorph. NF*, *21*, 57-78.

Heine, K., 1994. Present and Past Geocryogenic Processes in Mexico. *Permafrost and Periglacial Processes,* Vol. 5(1): 1-12.

Herrera, G., y Ruiz, J., 2009. Retroceso glaciar en la Sierra Nevada del Cocuy, Boyacá-Colombia, 1986-2007. Perspectiva Geográfica. Vol. 13: 27-36.

Huggel, C., Fischer, L., Schneider, D., Haebeerli, W., 2010. Research advances on climate-induced slope instability in glacier and permafrost high-mountain environments. Geographica Helvetica (65): 146-156.

Instituto Nacional de Estadística, Geografía e Informática, INEGI, 2017. Anuario estadístico y geográfico de los Estados Unidos Mexicanos. INEGI c2017. Aguascalientes, Ags. 1066 pp.

International Permafrost Association, IPA, 2008. Manual for Monitoring and Reporting Permafrost Measurements, Part 1: Permafrost Borehole Temperatures and Part II Active Layer, draft. http://www.permafrostwatch.org/.

Janke, J. R., Williams, M. W., Evans Jr., A., 2011. A comparison of permafrost prediction models along a section of trail Ridge Road, Rocky Mountain National Park, Colorado, USA. Geomorphology. doi: 10.1016/j.geomorph.2011.08.029.

Julián, A., y Chueca, J., 2004. "El permafrost esporádico de la cara norte de la Sierra de Telera (Pirineo Aragonés)" en J.L. Peña, L.A. Longares y M. Sánchez (ed.), *Geografía Física de Aragón. Aspectos generales y temáticos.* Universidad de Zaragoza e Institución Fernando el Católico. Zaragoza, España.

Julián, A. y Chueca, J., 2005. Modelización de la distribución del permafrost en la Sierra de Telera (Pirineo central español) a partir del empleo de Sistemas de Información Geográfica en *Rev. C. and G.* Vol. 20, Núm. 1-2, pp. 25-46.

Liang, S., 2000. Narrowband to broadband conversions of land surface albedo algorithms. Remote Sensing of Environment 76, 213-238.

Liang, S., Shuey, C. J., Russ, A. L., Fang, H., Chen, M., Walthall, C. L., ... & Hunt Jr, R., 2002. Narrowband to broadband conversions of land surface albedo: II. Validation. *Remote Sensing of Environment*, *84*(1), 25-41.

Liang, S. L., K. C. Wang, X. T. Zhang, and M. Wild, 2010. Review on estimation of land surface radiation and energy budgets from ground measurement, remote sensing and model simulations, IEEE J. Sel. Top. Appl. Earth Obs. Remote Sens., 3(3), 225–240, doi:10.1109/ jstars.2010.2048556.

Lorenzo, J. L., 1969a. Condiciones periglaciares de las altas montañas de México, Instituto Nacional de Antropología e Historia. *Peleoelología*, 4: 1-45.

Lorenzo, J. L., 1969b. Minor periglacial phenomena among the high volcanoes of Mexico. *The periglacial environment: past and present*, 161-175.

Macías, J. L., 2005. Geología e historia eruptiva de algunos de los grandes volcanes activos de México. *Boletín de la Sociedad Geológica Mexicana*, *57*(3), 379-424.

Macías, J.L., 2007. Geology and eruptive history of some active volcanoes of México, in Alaniz-Álvarez, S.A., and Nieto-Samaniego, Á.F., eds., Geology of México: Celebrating the Centenary of the Geological Society of México: Geological Society of America Special Paper 422, p. 183–232, doi: 10.1130/2007.2422(06).

Motulsky, H. J., and Christopoulos, A., 2003. Fitting models to biological data using linear and nonlinear regression, A practical guide to curve fitting, GraphPad Software Inc., San Diego, CA. USA. 351 pp.

Noetzli, J., Hoelzle, M., & Haeberli, W., 2003. Mountain permafrost and recent Alpine rock-fall events: a GIS-based approach to determine critical factors. In *Proceedings of the 8th International Conference on Permafrost* (Vol. 2, pp. 827-832). Swets & Zeitlinger Lisse, Zürich.

Organización Meteorológica Mundial, OMM., 2011. Guía de prácticas climatológicas No. 100. ISBN 978-92-63-30100-0. Ginebra, Suiza. 128 pp.

Osterkamp, T. E., & Jorgenson, M. T., 2009. Permafrost conditions and processes. *Geological monitoring: Geological Society of America*, 205-227.

Palacios, D., Zamorano, J. and Andrés, N., 2007. "Permafrost Distribution in Tropical Stratovolcanoes: Popocatépetl and Iztaccíhuatl Volcanoes (Mexico)" in *Geophysical Research Abstracts*. Vol. 9, 05615.

Rossotti, A., Carrasco-Núñez, G., Rosi, M., & Di Muro, A., 2006. Eruptive dynamics of the "Citlaltépetl pumice" at Citlaltépetl volcano, eastern Mexico. *Journal of Volcanology and Geothermal Research*, *158*(3-4), 401-429.

Serrano, E., Morales, C., González-Trueba, J. y Martín, R., 2009. "Cartografía del permafrost de montaña en los pirineos españoles" en *Finisterra*. Vol. XLIV, Núm. 87, pp. 45-54.

Smith, M. W., & Riseborough, D. W., 2002. Climate and the limits of permafrost: a zonal analysis. *Permafrost and Periglacial Processes*, *13*(1), 1-15.

Spehn, Eva; Berge, Erling; Bugmann, Harald; Groombridge, Brian; Hamilton, Lawrence; Hofer,Thomas; Ives, Jack; Jodha, Narpat; Messerli, Bruno; Pratt, Jane; Price, Martin; Reasoner, Mel; Rodgers, Alan; Thonell, Jillian; Yoshino Masatoshi., 2005. Mountain Systems. *In* Hassan, Rashid; Scholes, Robert and Ash Neville (edts) Ecosystems and Human Well-being: Current State and Trends, Volume 1. Island press, Washington, DC. 901 pp.

Trombotto, D., Wainstein, P., Arenson, L., 2014. Guía Términológica de la Geocriología Sudamericana. Terminological Guide of the South American Geocryology.Vázquez Mazzini EditoresFundación de Historia Natural, Buenos Aires. 128 pp.

Van Everdingen, R.O., 1985. Unfrozen permafrost and other taliks, In: Brown, J., Metz, M. C. and Hoekstra, P. (eds), Proceedings of the Workshop on Permafrost Geophysics, US Army, CRREL, Special Report, 85-5, 101–105.

Vosteen, H. D., & Schellschmidt, R., 2003. Influence of temperature on thermal conductivity, thermal capacity and thermal diffusivity for different types of rock. *Physics and Chemistry of the Earth, Parts A/B/C*, *28*(9-11), 499-509.

Williams, Peter, J., and Smith Michael W., 2008.The frozen earth, Fundamentals of geocrynology. Cambrridge University Press. Cambridge, Uk. 323 pp.

Williams Jr., R. S., 2012. Changes in the earth´s cryosphere and global environmental change. *In* Williams Jr., Richard S. And Ferrigno, Jane (edts). State of the Earth´s Cryospherre at the Beginning of the 21st Century: Glaciers, Global Snow Cover, Floating Ice, and Permafrost and Periglacial Envoronments. U.S. Geologycal Survey Professional Paper 1386-A. 496 pp.

Woodcock, A. H., 1974. Permafrost and climatology of a Hawaii volcano crater. *Arct. Alp. Res.*, 6(1): 49-62.

Yoshikawa, K. (ed.), 2013. *Permafrost in our time: community-based permafrost temperature archive*. University of Alaska Fairbanks Permafrost Outreach Program.